Symposium on Fluid-Structure Interaction and Aeroelasticity,
ASME Winter Annual Meeting, Chicago, IL, November 11, 1994.

EULERIAN-LAGRANGIAN SIMULATIONS OF TRANSONIC FLUTTER INSTABILITIES

Oddvar O. Bendiksen
Associate Professor
Department of Mechanical, Aerospace and Nuclear Engineering
University of California, Los Angeles, CA

ABSTRACT

This paper presents an overview of recent applications of Eulerian-Lagrangian computational schemes in simulating transonic flutter instabilities. n this approach, the fluid-structure system is treated as a single continuum dynamics problem, by switching from an Eulerian to a Lagrangian formulation at the fluid-structure boundary. This computational approach effectively eliminates the phase integration errors associated with previous methods, where the fluid and structure are integrated sequentially using different schemes. The formulation is based on Hamilton's Principle in mixed coordinates, and both finite volume and finite element discretization schemes are considered. Results from numerical simulations of transonic flutter instabilities are presented for isolated wings, thin panels, and turbomachinery blades. The results suggest that the method is capable of reproducing the energy exchange between the fluid and the structure with significantly less error than existing methods. Localized flutter modes and panel flutter modes involving traveling waves can also be simulated effectively with no a priori knowledge of the type of instability involved.

NOMENCLATURE

a = speed of sound; also location of elastic axis
c = 2b = airfoil chord
e = internal energy
E = total energy
f = body force
h = bending deflection, positive down
k = ωb/U= reduced frequency
K_h = typical section bending stiffness
K_α = typical section torsional stiffness
m = mass per unit span
M = Mach number
p = pressure

q_i = generalized coordinates
r = position vector
r_α = nondimensional radius of gyration about EA
s = blade spacing along leading edge locus
s_1 = $s \sin\theta$
s_2 = $s \cos\theta$
t = time
T = stress vector
T = kinetic energy
x_α = nondimensional CG-EA offset
u,v = velocities in x,y directions
u = material velocity vector
U = mesh velocity vector
$\bar{U}$ = $U_\infty/b\omega_\alpha$
U = strain energy
U_∞ = free-stream velocity at upstream infinity
α = angle of attack; also torsional deflection
θ = stagger angle; also node rotation
μ = $m/\pi\rho b^2$= mass ratio
ρ = air density
σ = interblade phase angle
ω = circular frequency, rad/s
ω_h = uncoupled frequency in bending
ω_α = uncoupled frequency in torsion

Superscripts and Subscripts
E = elastic
F = fluid
∞ = conditions at upstream infinity
e = conditions at exit

INTRODUCTION

The classical analytical methods and computational schemes for solving fluid-structure interaction problems were established in a different era, before the dawn of the computer age. Early developments in the field of unsteady aerodynamics, especially the exact solution of Theodorsen [1] for two-dimensional incompressible flow over an airfoil executing simple harmonic motion, undoubtedly influenced the direction of research. Thus, it not surprising that modal methods in the frequency domain played such a central role in the theoretical treatments of flutter calculations in the classical and modern texts on aeroelasticity [2-5].

Recent advances in supercomputers and massively parallel machines have had a significant impact on the feasibility of carrying out nonlinear transonic flutter calculations in the time-domain. It was pointed out by the author in Ref. 6 that this increased use of computers to simulate the behavior of physical systems has focused attention on the need to reexamine the existing classical approaches to certain problems. The frequency domain is a natural setting for problems amenable to the Fourier-type solution methods characteristic of classical unsteady aerodynamics, but not for nonlinear aeroelastic problems where the aerodynamic forces are computed in the time domain. Although time-domain aeroelastic calculations have by now become commonplace, the computational approach followed in most of these studies are along classical lines. That is, the fluid and the structure are modeled separately, and then coupled by specifying the kinematic boundary conditions at the fluid-structure boundary. The kinetic or natural boundary conditions are not treated as boundary conditions in the ordinary sense; instead, they provide forcing terms in the governing equations of motion for the structure.

This *classical approach* appears, at first glance, as a natural extension of the analytical frequency-domain methods into the computational time-domain. But on closer examination, a most important and fundamental difference emerges. Because the boundary between the fluid and the structure is a Lagrangian surface, whose state (displacements and velocity) must be known in order to impose the kinematic boundary conditions at this surface, the classical time marching method cannot be carried out without introducing approximations. The reason why approximations are necessary follows from the observation that in order to determine the exact state of the boundary at time t, one must first solve the entire system of equations for the structure. But this cannot be done until the surface pressure is known, which depends on the solution for the fluid domain, which in turn depends on the (yet unknown) boundary conditions during the current time step Δt. Thus, there can never be exact simultaneity between the unsteady events calculated in the structural and fluid domains. Since the fluid and the structure are in effect integrated sequentially during each time step, often using different numerical schemes, undesirable phase and integration errors are introduced.

There is thus a fundamental difference between *aeroelastic simulations*, where the structure is free to move in accordance with Newton's Laws, and steady or unsteady flow calculations, where the structure is fixed or forced to move in a *kinematically constrained* manner. This fact is seldom mentioned in papers dealing with computational fluid dynamics (CFD), or with the computational aspects of aeroelasticity. In unsteady flow calculations where the motion of the airfoil is prescribed, the future state of the fluid-structure boundary is known and numerical errors (whatever their source) do not affect the future position and motion of the boundary. Because the motion of the structure is unaffected by conformity or consistency errors arising at the fluid-structure boundary, such errors tend to "average out" over a cycle of oscillation. This *is not* the case in aeroelastic calculations, however. Not only is the future state of the fluid-structure boundary unknown, causing the aforementioned difficulty in implementing the boundary conditions, but errors from all sources affect the future position and velocity of the fluid-structure boundary. The computational model of the aeroelastic system behaves as a feedback control system, where the state of the structural system is not only affected by the "true" aerodynamic forces, but also by fictitious "control forces" arising from the continued feedback of modeling and numerical errors. Here, errors do not tend to "average out" over a cycle and remain bounded in the long run, because of the highly nonlinear amplification possible through this feedback mechanism.

Results from a large number of numerical simulations of transonic flutter instabilities indicate that two distinctly different manifestations of these errors can occur:

1. A long-term cumulative error in the calculated motion of the aeroelastic system, similar to the temporal nonuniformities or far-field nonuniformities that occur in perturbation problems that are singular or involve multiple time scales.
2. A significant qualitative and quantitative error in the stability behavior of the system, including a large error in the calculated flutter boundary and possibly also a qualitatively incorrect assessment of the type of instability behavior (flutter vs. divergence).

It should be clear from these observations that one must distinguish between the inherent accuracy of the individual CFD and FEM computational schemes used for the fluid and solid domains, and the accuracy of the overall aeroelastic scheme. It is meaningless to insist on higher-order CFD/FEM schemes in flutter calculations if the boundary conditions are implemented such that only first-order (or less!) accuracy is obtained in the aeroelastic simulations. The implications for implicit schemes, where the allowable time step Δt is set by accuracy rather than numerical stability considerations, are obvious.

In Ref. 6, we have proposed a new approach to the problem, which has been further developed and explored in a series of papers [7-11]. By formulating the governing equations for both the fluid and the structure in integral conservation-law form based on the same mixed Eulerian-Lagrangian description, the entire fluid-structure system can be treated as *one* problem, while still allowing for different spatial discretization schemes in the two domains, if so desired. In this approach, the boundary conditions become transparent to the time-marching

algorithm, resulting in highly vectorizable codes. The method also provides a systematic and efficient procedure for coupling finite element structural codes to finite volume or finite element fluid codes, allowing the direct use of highly accurate finite element structural models rather than a truncated set of normal modes.

The objective of the present paper is to present a brief overview of the computational method, and to illustrate its application in distinctly different areas of classical and computational aeroelasticity. The transonic flow regime is intentionally emphasized, because of the challenges it represents both from a computational fluid dynamics standpoint, and also because of its rich source of nonlinear and surprising aeroelastic phenomena. These cases include illustrations of aeroelastic instabilities where several degrees of freedom participate to generate localized response or traveling waves, which are difficult to treat accurately using modal methods.

VARIATIONAL FORMULATION OF AEROELASTIC CONSERVATION LAWS

Hamilton's Principle

Coupled fluid-structure interaction problems involve, by definition, interactions between two distinct material domains (fluid and solid). In modeling the structural problem, finite element methods based on a Lagrangian (material) description are typically used, and Hamilton's Principle and variational methods play an important role in formulating the equations of motion. For the fluid problem, finite difference or finite volume methods based on an Eulerian (spatial) description are more popular, and variational methods are conspicuous in their absence.

If Eulerian coordinates are used in connection with the classical Lagrangian density, Hamilton's Principle gives trivial results. Various attempts have been made to augment the Lagrangian by adding terms that, when substituted into Hamilton's Principle will yield the sought field equations; see, for example, the discussion in Ref. 12. Although many of these investigations take Hamilton's Principle as a starting point, they usually have little if anything to do with the physical contents of the principle.

Hamilton's Principle represents an alternate formulation of Newtonian mechanics, and is therefore capable of producing the correct equations of motion in an arbitrary coordinate system. There is no need to introduce *ad hoc* terms in the Lagrangian, a procedure that this author considers in violation of the spirit of Hamilton's Principle. One must recognize, however, that Hamilton's Principle is based on material particles and variations of the Newtonian paths of such particles, and that the *mass* of a particle is not to be varied in the process of varying the path.

To this end, we introduced in Ref. 7 the concept of a "material variation", constructed such that the variational operator δ in Hamilton's Principle remains a Newtonian path variation under coordinate transformations. Consider a finite region of a continuum, represented by a material cell of volume Ω, as illustrated in Fig. 1. Hamilton's Principle in its extended form,

$$\int_{t_1}^{t_2} [\,\delta T - \delta U + \delta W_E\,]\, dt = 0 \tag{1}$$

is applicable without additional assumptions regarding the nature of the forces present. Here, δW_E is the virtual work of all forces acting on the material particles in the volume, and may include forces for which no scalar potential can be found such that $\delta W_E = -\delta V$. In this very general form, the principle is an integral statement of D'Alembert's Principle rather than a "true" variational principle.

If all forces are derivable from scalar potentials, Eq. (1) becomes a variational principle:

$$\delta \int_{t_1}^{t_2} L\, dt = \delta \int_{t_1}^{t_2} \int_{\Omega} L_0\, d\Omega\, dt = 0 \tag{2}$$

This form is well-established for conservative dynamical systems; however, it is also valid for nonconservative systems where the Lagrangian is time-dependent, as long as the previous assumptions hold.

The Lagrangian density L_0 is defined as

$$L_0 = T_0 - U_0 - V_{0_E} = T_0 - V_0 \tag{3}$$

where

$$T_0 = \frac{1}{2}\rho \dot{\eta}_i \dot{\eta}_i + T_0^1(\eta_i, \dot{\eta}_i) + T_0^0(\eta_i) \tag{4a}$$

$$U_0 = \int_0^{\varepsilon_{ij}} \sigma_{ij}\, d\varepsilon_{ij} \tag{4b}$$

Here, T_0 and U_0 are the kinetic and internal energy densities, respectively. The terms T_0^0 and T_0^1 are only present in noninertial reference frames and give rise to centripetal and Coriolis forces. The coordinates η_i are arbitrary generalized displacement coordinates, in the distributed sense. Finally, V_{0_E} is the density associated with the potential of the external forces,

$$\nabla V_E = \int_{\Omega} \nabla V_{0_E}\, d\Omega \tag{5a}$$

$$\rho f = -\nabla V_{0_E} \tag{5b}$$

For a solid element, U_0 is the familiar strain energy density. For a fluid element, U_0 is equal to the (intrinsic) internal energy per unit volume, which for a perfect gas reduces to

$$U_0 = \frac{1}{\gamma - 1} p \tag{6a}$$

$$\rho e = U_0 + T_0 \tag{6b}$$

where e is the total energy per unit mass. In either case, U_0 represents the internal potential energy, and Eq. (6a) is obtained from Eq. (4b) by assuming inviscid flow, $\sigma_{ij} = -p\delta_{ij}$, and integrating along a reversible path, using the perfect gas law.

Euler-Lagrange Equations of Motion

For inviscid flows, it suffices to consider variations of "action" integrals of the form

$$I = \int_{t_1}^{t_2} \int_{\Omega(t)} L_0(x_i, t, \eta_i, \eta_{i,j}, \dot{\eta}_i)\, d\Omega dt \tag{9}$$

where the η_i's represent arbitrary generalized displacement coordinates in the distributed sense. In Lagrangian coordinates, applying Hamilton's Principle by setting $\delta I = 0$ (Ω fixed) leads to the classical Euler-Lagrange equations of the calculus of variations:

$$\frac{\partial L_0}{\partial \eta_i} - \frac{\partial}{\partial t}\frac{\partial L_0}{\partial \dot{\eta}_i} - \frac{\partial}{\partial x_j}\left(\frac{\partial L_0}{\partial \eta_{i,j}}\right) = 0 \tag{10}$$

In a mixed Eulerian-Lagrangian description, the domain $\Omega(t)$ constitutes an intermediate reference frame, moving with an arbitrary but kinematically specified velocity $\boldsymbol{U}$. Consider the material integral

$$\Phi = \int_{\Omega(t)} \phi(x_i, t, \eta_i, \eta_{i,j}, \dot{\eta}_i)\, d\Omega \tag{11}$$

The time rate of change of Φ in the x_i reference frame is

$$\frac{d\Phi}{dt} = \int_{\Omega(t)} \left\{ \frac{\partial \phi}{\partial t} + \nabla\cdot[(\boldsymbol{u} - \boldsymbol{U})\phi] \right\} d\Omega \tag{12}$$

and may be considered a total or convective rate. It is then straight-forward to show that, in order to preserve the material nature of the variational operator "δ" in Hamilton's Principle, the time derivative in the classical Euler-Lagrange equations must be changed as follows:

$$\frac{\partial}{\partial t}(\cdot) \rightarrow \frac{\partial}{\partial t}(\cdot) + \nabla\cdot[(\boldsymbol{u} - \boldsymbol{U})(\cdot)] \tag{13}$$

The corresponding (modified) Euler-Lagrange equations, valid in arbitrary mixed cartesian coordinates, become

$$\frac{\partial L_0}{\partial \eta_i} - \frac{\partial}{\partial t}\frac{\partial L_0}{\partial \dot{\eta}_i} - \frac{\partial}{\partial x_j}\left[(u_j - U_j)\frac{\partial L_0}{\partial \dot{\eta}_i} + \frac{\partial L_0}{\partial \eta_{i,j}}\right] = 0 \tag{14}$$

In an inertial coordinate system x_i in the absence of body forces, $\partial L_0/\partial \eta_i = 0$ (translational invariance). The following conservation-law form of Eq. (14) is then obtained:

$$\frac{\partial}{\partial t}\frac{\partial L_0}{\partial \dot{\eta}_i} + \frac{\partial}{\partial x_j}\left[(u_j - U_j)\frac{\partial L_0}{\partial \dot{\eta}_i} + \frac{\partial L_0}{\partial \eta_{i,j}}\right] = 0 \tag{15}$$

Recognizing that the velocity field is given by $u_i = \dot{\eta}_i$,

$$\frac{\partial L_0}{\partial \eta_i} = \rho f_i \;; \qquad \frac{\partial L_0}{\partial \dot{\eta}_i} = \rho u_i \tag{16}$$

and because of the symmetry of the strain tensor ε_{ij}, it follows that

$$\frac{\partial L_0}{\partial \eta_{i,j}} = -\frac{\partial U_0}{\partial \eta_{i,j}} = -\frac{\partial U_0}{\partial \varepsilon_{ij}} = -\sigma_{ij} \tag{17}$$

The governing equations (14) can thus be written as

$$\frac{\partial}{\partial t}(\rho u_i) + \frac{\partial}{\partial x_j}[(u_j - U_j)\rho u_i - \sigma_{ij})] = \rho f_i \tag{18}$$

valid in an inertial cartesian coordinate system x_i. For an inviscid fluid, the stress tensor is diagonal

$$\sigma_{ij} = -p\,\delta_{ij} \tag{19}$$

and we obtain the Euler equations of fluid mechanics by setting $U_j = 0$. If one sets $u_j = U_j$, the Lagrangian form of the equations of motion are obtained (the divergence is readily expressed in terms of Lagrangian coordinates; see, for example, Lamb [13].)

We note in passing that the corresponding Navier-Stokes equations can be obtained by substituting into Eq. (18) the constitutive law

$$\sigma_{ij} = -p\delta_{ij} + 2\mu(e_{ij} - \frac{1}{3}\Delta\delta_{ij}) \tag{20}$$

where μ here is the viscosity and

$$e_{ij} = \frac{1}{2}(u_{i,j} + u_{j,i}) \quad ; \quad \Delta = e_{kk} \tag{21}$$

are the strain rates and the volumetric expansion rate, respectively.

The conservation of mass equation is a *kinematic* constraint, and is readily incorporated into the variational formalism using a Lagrange multiplier. In the present paper, the integral form is used in the actual discretization procedure,

$$\frac{\partial}{\partial t}\int_\Omega \rho\, d\Omega + \int_{\partial\Omega} \rho\,(u_i - U_i)\, n_i\, dS = 0 \tag{22}$$

In most cases in aeroelasticity, the energy equation can be handled in a similar manner, since in cases where only mechanical energies are involved, it is simply a first integral of the equations of motion. In integral form, it reads

$$\frac{\partial}{\partial t}\int_\Omega \rho e\, d\Omega + \int_{\partial\Omega} \rho e\,(u_i - U_i)\, n_i\, dS = \int_\Omega \rho u_i f_i\, d\Omega + \int_{\partial\Omega} u_i T_i^n\, dS \tag{23}$$

where f_i and T_i^n are the cartesian components of the body forces and surface tractions, respectively. The components T_i^n are related to the stress tensor through the relation

$$T_i^n = \sigma_{ij}\, n_j \tag{24}$$

It is convenient and useful to integrate the energy equation and use the relation

$$p = (\gamma - 1)[\,\rho e - T_0\,] \tag{25}$$

to eliminate the pressure p. For a solid cell, such an elimination is not generally possible, because the internal energy depends on all six components of the stress tensor.

Boundary Conditions

In the classical method of numerically solving fluid-structure interaction problems, only the kinematic boundary condition of tangent flow is imposed:

$$\frac{\partial B}{\partial t} + \boldsymbol{u}\cdot\nabla B = 0 \tag{26}$$

where $B(x,y,z,t) = 0$ defines the instantaneous locus of the fluid-structure boundary. The kinematic boundary conditions are not enforced explicitly; that is, one does not enforce local force equilibrium between a fluid and a solid element at the boundary B, nor does one equate the energy flow or power at the common boundary.

In the present study, both kinematic and kinetic boundary conditions are satisfied *locally* at the fluid-structure boundary. By switching from an Eulerian to a Lagrangian formulation at the boundary, the boundary conditions become transparent and they can be satisfied automatically as the equations of motion are integrated. The kinematic boundary condition can be imposed by zeroing out the convective fluxes at the fluid-structure boundary, leaving only the pressure terms in the boundary integrals. These pressure terms contribute to the kinetic boundary conditions, but need not be considered explicitly because the kinetic boundary conditions between cells are taken care of by the conservation laws being integrated.

At the upstream and downstream far-field boundaries we use nonreflecting boundary conditions of the type formulated by Hedstrom [14] and generalized to two space dimensions in Ref. 15. In the cascade calculations, phase-lagged periodic boundary conditions are applied at the boundaries of the reference channel. Thus, if ξ denotes the spatial coordinate along the periodic (upper and lower) boundaries of the reference channel, we enforce

$$W_l(\xi, t) = W_u(\xi, t - \sigma/\omega) \tag{27a}$$

$$W_u(\xi, t) = W_l(\xi, t - (2\pi - \sigma)/\omega) \tag{27b}$$

where σ and ω are the interblade phase angle and the circular frequency, and the subscripts u and l indicate upper and lower boundaries, respectively. In order to prevent numerical instabilities, it is necessary to limit the magnitude of the change in the periodic boundary conditions during each time step.

SPATIAL DISCRETIZATION SCHEMES

Finite Volume Method

In the two-dimensional cases considered in this paper, we take the unknowns as

$$W = \begin{Bmatrix} \rho \\ \rho u \\ \rho v \\ \rho e \end{Bmatrix} \tag{28}$$

Applying the divergence theorem to the Euler-Lagrange equations, with the mass and energy equations appended, the system is transformed into the following set of integral conservation laws:

$$\frac{\partial}{\partial t}\int_{\Omega} W dx dy + \int_{\partial\Omega} (F_x n_x + F_y n_y) ds = 0 \tag{29}$$

where Ω is an element area with (moving) boundaries $\partial\Omega$ and

$$F_x = \begin{Bmatrix} \rho(u-U) \\ \rho u(u-U) - \sigma_{nn} \\ \rho v(u-U) - \sigma_{ns} \\ \rho e(u-U) - \sigma_{nn} u - \sigma_{ns} v \end{Bmatrix} \qquad F_y = \begin{Bmatrix} \rho(v-V) \\ \rho u(v-V) + \sigma_{ns} \\ \rho v(v-V) - \sigma_{nn} \\ \rho e(v-V) + \sigma_{ns} u - \sigma_{nn} v \end{Bmatrix} \tag{30}$$

Here, u,v and U,V are the cartesian components of $\boldsymbol{u}$ and $\boldsymbol{U}$, respectively, and σ_{nn} and σ_{ns} are the normal and shear stresses at the surface $\partial\Omega$. For a cell occupied by an inviscid fluid, we set $\sigma_{nn} = -p$, $\sigma_{ns} = 0$ and use Eq. (25) to eliminate the pressure.

By applying the integral form of the conservation laws to each fluid cell, we obtain a system of coupled ordinary differential equations of the form

$$\frac{d}{dt}(\Omega_{ij} W_{ij}) + Q_{ij} - D_{ij} = 0 \tag{31}$$

where Ω_{ij} is the cell area, W_{ij} is the vector of unknowns for cell (i,j), and Q_{ij} is the net flux out of the cell (i,j), contributed by the integral over $\partial\Omega$ in Eq. (29). The flow variables are assumed constant over each cell and are averaged at cell edges, resulting in second-order accuracy on a smooth mesh. D_{ij} is a dissipative operator added to damp out numerical oscillations and to prevent decoupling of even and odd cells. The dissipative fluxes are constructed according to the idea of "adaptive dissipation" developed by Jameson and Baker [16], using a blend of second and fourth differences in the flow variables.

Galerkin Finite Element Method

Two different finite element schemes are considered in this paper. The first scheme is closest to the finite volume procedure discussed in the previous section, wherein the divergence theorem is used (in reverse) to obtain the integral conservation-law form of the equations. The Galerkin finite element procedure is then applied to obtain space-discretized equations in the usual manner, by approximating the vector W of unknowns as

$$W(x,y,t) = \sum_j W_j(t)\,\phi_j(x,y) \tag{32}$$

where W_j are nodal values of W and ϕ_j are shape (interpolation) functions. In the present paper, linear interpolation functions are used and the solution is implemented using triangular elements.

The solution is obtained by discretizing the weak form of the equations,

$$\frac{\partial}{\partial t}\int_{\Omega} W\,\phi_i\, d\Omega + \int_{\Omega} \phi_i\, \nabla\cdot F\, d\Omega = 0 \tag{33}$$

where

$$F = F_x \hat{i} + F_y \hat{j} \tag{34}$$

and F_x and F_y are given by Eq. (30). Substituting Eq. (32) into the first term in Eq. (33) and interchanging the order of summation and integration, one obtains

$$\frac{\partial}{\partial t}\int_{\Omega}(\sum_j W_j\phi_j)\phi_i\,d\Omega = \frac{d}{dt}(\sum_j m_{ij}^{\Omega} W_j) \tag{35}$$

where

$$m_{ij}^{\Omega} = \int_{\Omega}\phi_i\phi_j\,d\Omega \tag{36}$$

are the elements of the consistent mass matrix, for element Ω. In the unsteady (deforming mesh) case, the mass matrix is time-varying and depends on the local Jacobian determinant. However, if linear shape functions are used, the generalized mass elements can be evaluated exactly.

Using the divergence theorem, the second term in Eq. (33) can be written as

$$\int_{\Omega}\phi_i\,\nabla\cdot\boldsymbol{F}\,d\Omega = \int_{\partial\Omega}\phi_i\,\boldsymbol{F}\cdot\boldsymbol{n}\,dS - \int_{\Omega}\boldsymbol{F}\cdot\nabla\phi_i\,d\Omega \tag{37}$$

where $\boldsymbol{n}$ is the unit outward normal to the boundary $\partial\Omega$ of Ω. Because $\boldsymbol{F}$ is a nonlinear function of the flow variables, the integrals in Eq. (37) must be evaluated numerically. Denoting the contribution by the flux integrals, Eq. (37), associated with node i of element Ω by Q_i^{Ω}, the space-discretized FE equations of motion for *a single element* become

$$\frac{d}{dt}(\sum_j m_{ij}^{\Omega} W_j) + Q_i^{\Omega} = 0 \tag{38}$$

where the range of the i and j indices are the nodes for element Ω.

Equations (38) are formally identical to the corresponding FE equations for a structural element, if the W_i's and the Q_i^{Ω}'s are interpreted as the element generalized coordinates and the corresponding (nodal) generalized forces, respectively. But in the present formulation, we do not assemble the element matrices into global system matrices, as is customary in structural dynamics. Instead, we perform a *local assembly* only, by algebraically summing the contributions from all elements Ω_k^i that meet at node i. The union of these elements forms a control volume V_i surrounding node i; hence this local assembly can also be performed by applying the above finite element discretization equations directly to the "superelements"

$$V_i = \sum_{k=1}^{N_i}\Omega_k^i \quad ; \quad i = 1, 2, \cdots, N \tag{39}$$

where N_i is the number of elements meeting at node i and N is the total number of nodes. Adding dissipative terms, the space-discretized Galerkin FE equations can be written as

$$\frac{d}{dt}(\sum_j m_{ij} W_j) + Q_i - D_i = 0 \tag{40}$$

where $i = 1, 2, \cdots N$ (all nodes), and the summation on j extends over the nodes in the superelement V_i associated with node i. The dissipative fluxes D_i are of the Jameson type, and are slight modifications of the terms used by Mavriplis [17] in his nodal finite volume code. In

the FE calculations presented in this paper, unstructures triangular grids of the type illustrated in Fig. 2 were used. Slightly different implementations were used in the external (panel) and the internal (cascade) calculations; see Refs. 18-19 for further details.

Lagrangian Finite Element Method

The second scheme proceeds directly from the variational principle (Hamilton's) to the discretized Lagrange equations in a suitable set of generalized coordinates, $\{q\}_{ij}$. This is the procedure used to obtain the space-discretized equations for the solid domain (wing, blades, panel). At the fluid-structure boundary, we switch from a mixed method to a Lagrangian method by setting $U_i = u_i$.

Modified Typical Section. A typical section isolated wing model has been implemented as illustrated in Fig. 3. A section of unit width in the spanwise direction is considered, in the spirit of the original ideas of Theodorsen and Garrick, but with two important differences. First, the section is allowed to have camber bending, and this "chordwise" flexibility is modeled using plate-type elements of unit width; see Fig. 3b. Each element is allowed a hollow core, by specifying the effective structural skin thickness t_s for each element. Second, since the method of calculation is at the element level, an attempt is made to model the distributed restraining stiffness from the remainder of the wing on each element, by introducing bending and torsion springs at the element nodes. By careful tailoring of the parameters as discussed in Ref. 6, the strip model can be matched to any regular typical section model in the limit as the chordwise stiffness approaches infinity.

On a C-mesh of quadrilateral elements, one obtains a set of discretized equations very similar to Eqs. (31):

$$\frac{d}{dt}([m]_{ij}\{\dot{q}\}_{ij}) + \{Q^E\}_{ij} - \{Q^F\}_{ij} = 0 \tag{41}$$

Here, the i,j subscripts refer to the (i,j) node, whereas elements are labeled with superscripts; i.e., $[m]^{ij}$ is the *element* mass matrix. For the blade structure in Fig. 3, the structural elements are at j=1, and we can drop the j-subscript and write

$$\{q\}_i^T = \{\, w_i \;\; \theta_i \,\} \tag{42}$$

where w_i and θ_i are the transverse and rotational displacements at node $(i, 1)$, Fig. 3b. Plate element of unit width are used, with the transverse displacement $w(\xi,t)$ inside a typical element approximated in terms of the nodal coordinates q_k as follows:

$$w(\xi,t) = \sum_{k=1}^{4} N_k(\xi) q_k(t) \tag{43}$$

where the N_k's are the standard cubic shape functions.

The 2x2 "nodal" mass matrix in Eq. (41) is written in terms of the lumped element mass matrices for elements i and i+1 as

$$[m]_i = [m]_{22}^{i} + [m]_{11}^{i+1} \tag{44}$$

where the element matrices have been partitioned into 2x2 submatrices in the usual way. Similarly, the nodal elastic forces $\{Q^E\}_{ij}$, and the generalized nodal fluid pressure forces

$\{Q^F\}_{ij}$ can be expressed in terms of the corresponding element forces, as follows:

$$\{Q^E\}_i=([k]^i_{22}+[k]^{i+1}_{11})\{q\}_i+[k]^i_{21}\{q\}_{i-1}+[k]^{i+1}_{12}\{q\}_{i+1} \tag{45}$$

$$Q^F_{1i}=Q^{F(i+1)}_1+Q^{Fi}_3 \tag{46a}$$

$$Q^F_{2i}=Q^{F(i+1)}_2+Q^{Fi}_4 \tag{46b}$$

where

$$Q^{Fi}_k=\int_0^{l_k} N_k(\xi)[p^i_l(\xi)-p^i_u(\xi)]\,d\xi \tag{47}$$

and p^i_l and p^i_u are the fluid pressures on the lower and upper surfaces of the *ith* element, respectively. It is important to note that we do not need to assemble the structure and form global stiffness (or mass) matrices; only *local* assembly at the element (node) level is required, precisely as in the fluid domain. Although we have assumed a linearly elastic structure in Eq. (45), nonlinear material behavior, both elastic and inelastic, are relatively easy to incorporate at the local element level.

To complete the solution procedure, we need to perform another integration to get from $\{\dot{q}\}$ to $\{q\}$. This is necessary since we need to know the actual nodal displacement vectors in order to move the mesh coordinates x_{ij}, y_{ij} in a Lagrangian fashion. It is done simultaneously in the multi-stage Runge-Kutta scheme, by writing the equations in state-variable form by appending at each node the matrix identity

$$\frac{d}{dt}\{q\}_{ij}=\{\dot{q}\}_{ij} \tag{48}$$

The energy equation for the structure is discretized and integrated as follows

$$\frac{d}{dt}(E_{tot})=\dot{E}_{tot}=\sum_i\{\dot{q}\}^T_i\{Q^F\}_i \tag{49}$$

where

$$E_{tot}=\sum_i(T_i+U_i) \tag{50}$$

For a linearly elastic structure, the kinetic and strain energies can be expressed in terms of the present (local) element mass and stiffness matrices as

$$T_i+U_i=\frac{1}{2}\{\dot{q}\}^T_i[m]_i\{\dot{q}\}_i+\frac{1}{2}\{q\}^T_i[k]_i\{q\}_i \tag{51}$$

From a computational standpoint, it is both natural and advantageous to use finite elements throughout both the structural and the fluid domains. By imposing "conformity" or "compatibility" conditions on the shape functions, we guarantee that the basic conservation laws for mass, momentum, and energy are satisfied at the fluid-structure boundary, to within the discretization error of the scheme. For maximum modeling flexibility and computational efficiency, both the fluid and the solid element should be allowed interior nodes with respect to the other. In modeling thin compressor blades with plate elements, as in the present scheme, we use a much coarser mesh for the structure, especially in the leading and trailing edge regions where flow gradients are high. By matching the mesh densities appropriately, a simultaneous optimization of the computational efficiency and the discretization/modeling errors can be achieved.

Rotating Turbomachinery Blade. The blade is modeled as a thin plate with varying thickness, using the von Karman theory to incorporate the effect of the in-plane centrifugal forces. The kinetic energy of the rotating blade, Fig. 4, can be expressed in the form

$$T = \frac{1}{2}\int \rho h\{\dot{w}^2 + \Omega^2[(r_0+y)^2 + (w\cos\theta + x\sin\theta)^2]\}dxdy \tag{52}$$

where term associated with Coriolis forces have been neglected. The total strain energy can be expressed as

$$U = \int U_0 dxdydz = U_b + U_a \tag{53}$$

$$U_b = \frac{1}{2}\int D\left[\left[\frac{\partial^2 w}{\partial x^2}\right]^2 + \left[\frac{\partial^2 w}{\partial y^2}\right]^2 + 2\nu\frac{\partial^2 w}{\partial x^2}\frac{\partial^2 w}{\partial y^2} + 2(1-\nu)\left[\frac{\partial^2 w}{\partial x \partial y}\right]^2\right]dxdy \tag{54a}$$

$$U_a = \frac{1}{2}\int [N_x\varepsilon_{x_0} + N_y\varepsilon_{y_0} + N_{xy}\gamma_{xy_0}]dxdy \tag{54b}$$

where $D = Eh^3/12(1-\nu^2)$ is the flexural rigidity of the plate, U_b is the bending strain energy, and U_a is the strain energy due to the in-plane centrifugal forces.

The stress resultants N_x, N_y, and N_{xy}, which arise from centrifugal forces and give rise to the strains ε_{x_0}, ε_{y_0} and γ_{xy_0} in the middle surface of the plate, are approximated as follows:

$$N_x = \int_x^b \rho h\Omega^2 \xi \sin^2\theta d\xi \tag{55a}$$

$$N_y = \int_y^L \rho h\Omega^2(r_0 + \eta)d\eta \tag{55b}$$

$$N_{xy} = 0 \tag{55c}$$

The virtual work done by the aerodynamic forces on the rotating blade is given by

$$\delta W_E = \int (p_l - p_u)\delta w dxdy = \sum_i Q_i^F \delta q_i \tag{56}$$

where p_l and p_u are the fluid pressures on the lower surface and the upper surface of the blade, respectively, and Q_i^F are the generalized fluid forces.

In the present study, the blade is discretized into $n \times m$ rectangular plate elements. For each element, a bi-cubic polynomial is used to describe the deflection field. The transverse displacement inside element ij can be expressed in local element coordinates (ξ,η) as:

$$w_{ij}(\xi,\eta,t) = \sum_{k=1}^{16} N_k(\xi,\eta)q_k(t) \tag{57}$$

where q_1–q_4, q_5–q_8, q_9–q_{12} and q_{13}–q_{16} are the nodal value of w, $\partial w/\partial x$, $\partial w/\partial y$, $\partial^2 w/\partial x \partial y$ associated with nodes 1, 2, 3 and 4. The shape functions $N_k(\xi,\eta)$ are products of the first-order one-dimensional Hermitian interpolation functions.

The space-discretized equations of motion for a given element or the entire blade can be obtained using Lagrange's equations, after substituting Eq. (57) into the appropriate expressions for T and U:

$$\frac{d}{dt}([M_2]\{\dot{q}\}) + ([K] - [M_0])\{q\} - \{Q^C\} - \{Q^F\} = 0 \tag{58}$$

where $\{q\}$ is the generalized coordinate vector of the discretized system, $[M_2]$ is the mass matrix associated with the part of the kinetic energy involving the quadratic terms of generalized speeds, while $[M_0]$ and $\{Q^C\}$ are related to the kinetic energy due to the centrifugal force. $[K]$ is the stiffness matrix including both the linear stiffness and nonlinear stiffness due to the in-plane stretching. For further details, see Ref. 20.

The complete aeroelastic model is shown schematically in Fig. 4b. The cantilever blade lies in x-y plane, where x indicates the chordwise direction and y indicates the spanwise direction; see also Fig. 4a. The shaded strips are the control channels, where we assume that the motion of the fluid is governed by the two-dimensional Euler equations in the x-z plane. The aerodynamic loads are computed inside each channel and interpolated linearly between adjacent channels. This channel theory can be interpreted as an extented (numerical) version of classical strip theory.

Nonlinear Panel. The structural model used in the two-dimensional panel flutter simulations is based on the nonlinear von Karman plate equations, which can be written as

$$D\frac{\partial^4 w}{\partial x^4} - (N_x + N_{x0})\frac{\partial^2 w}{\partial x^2} + \rho h\frac{\partial^2 w}{\partial t^2} = p_\infty - p \tag{59}$$

Here, N_{x0} is the initial in-plane loading due to external forces, and N_x is the additional in-plane force induced by the transverse deflections w:

$$N_x = \frac{Eh}{2c}\int_0^c (\frac{\partial w}{\partial x})^2 dx \tag{60}$$

where c is the plate chord length.

These equations can be discretized using standard finite element techniques, resulting in a set of governing equations of the same basic form as Eq. (41). In the present case, the elastic forces in the *ith* element can be expressed as a sum of two terms

$$\{Q^E\}^i = ([k]^i + [k_g]^i)\{q\}^i \tag{61}$$

where $[k]$ is the linear part of the stiffness matrix and $[k_g]$ is the so-called geometric stiffness matrix arising from the nonlinear stiffness caused by the in-plane stretching due to transverse deflections of the plate. It should be noted that, because of the fact that the geometric stiffness matrix is proportional to $(N_{x0} + N_x)$, this matrix depends on the deformations of all elements in the panel, as is obvious from Eq. (60). Expressions for these matrices can be found in Ref. 21.

NUMERICAL EXAMPLES

Sub-transonic flows ($M_{crit} < M_\infty < 1$) are characterized by local regions of embedded supersonic flow on the upper and/or lower surfaces of the airfoil. At the aft end of these regions, the flow is decelerated to subsonic speeds through nearly normal shock waves. During vibration and flutter, the shocks move along the airfoil surfaces, changing in strength and possibly vanishing over part of the cycle.

Because of the important role that shock motion plays in the flutter problem, a realistic simulation of transonic flutter instabilities cannot be achieved unless the moving shocks are treated correctly and in a time-accurate manner. Furthermore, in order to model a mixed subsonic-supersonic flow-field with finite-amplitude shock motion, nonlinear field equations are required. If the flow is not of the mixed type, i.e., is either entirely subsonic or entirely supersonic, the equations can usually be linearized for sufficiently small amplitudes of motion, or for sufficiently high reduced frequencies. In the mixed subsonic-supersonic (transonic) case, however, the linearization is subject to severe restrictions on blade amplitudes and may in some cases break down.

Transonic Flutter of Airfoils

Except as noted, we have used 5 finite elements in the chordwise direction; 3 elastic elements and two small rigid-body elements at the leading and trailing edges. An all aluminum structure was assumed, with t_s/t varied as noted on the figures.

Figure 5 compares the calculated bifurcation diagrams for the NACA 64A006 wing model ($\mu = 10$), as calculated using the present method and compared with results taken from Fig. 3 of Ref. 22, which were calculated using the classical approach, as implemented in Refs. 22-23. This model has also been studied extensively by Ashley [24]. In the notation used here, it has the following nondimensional parameters:

$$a = -0.2$$

$$x_\alpha = 0.2 \qquad (\chi_c = 0)$$

$$r_\alpha^2 = 0.29 \qquad (\rho_M^2 = 0.25)$$

$$\omega_h/\omega_\alpha = 0.3434 \qquad (\omega_w/\omega_\theta = \sqrt{0.1})$$

The corresponding equivalent parameter values in Ashley's notation have been indicated in parenthesis.

To provide meaningful comparisons, the fluid domain was modeled and solved in *exactly* the same manner as in Refs. 22-23, using the same mesh and the the same five-stage Runge-Kutta integration scheme. However, in the earlier method the structural equations were integrated *separately*, after the fluid equations had been advanced to the next stage within the multistage scheme. This necessitated an approximation for the lift and moment for the next time step, and a linear extrapolation was used in Refs. 22-23. In the present approach, no such approximation is necessary, since the entire domain of the continuum and all its cells are advanced simultaneously in time. That is, no distinction is made between solid and fluid cells during the actual time integration process.

From Fig. 5 it is evident that the *linear* flutter boundary, represented by the bifurcation points on the $\bar{U}$ axis, are in reasonable agreement. However, for this example at least, the classical method *underpredicts* the limit cycle amplitudes for reduced velocities significantly beyond the linear flutter boundary. The reason for this is that the method underpredicts the net energy flux from the fluid to the structure. Close to the linear flutter points, the results are less definite and show a greater sensitivity to the computational mesh. At a Mach number of .87, decreasing the chordwise stiffness of the model by decreasing the structural thickness ratio t_s/t has the effect of increasing the energy flow to the structure, resulting in an increase in the

flutter limit cycle amplitude. A comparison of the long-time limit cycle amplitudes is shown in Fig. 6. This camber bending effect appears negligible for ratios of 0.25 and higher, but become significant for t_s/t less than 0.1. This is in contrast to the same wing at $M = 0.92$, where chordwise flexibility initially (close to the flutter boundary) is *stabilizing*, then becoming mildly destabilizing as $\bar{U}$ is increased beyond 2.3.

For Mach numbers in the upper transonic range (0.9-1.0), the shocks are typically found to be confined to the trailing edge region of the airfoil. During flutter, the shocks do not move but change in strength, imposing a significant localized loading on the trailing edge. If the trailing edge is sufficiently flexible, the present model predicts that a local "trailing-edge buzz" mode can get excited, as illustrated in Fig. 7, where the trailing-edge region oscillates somewhat like a trailing-edge flap. Here, the Mach number is 0.92, $\bar{U} = 3.0$, and $t_s/t = 0.10$.

The term "buzz" is used here to suggest a high-frequency modulation of the flutter mode, and not necessarily to suggest any connection to the well-known phenomenon of "aileron buzz", where the viscosity is generally believed to play an important role, through a shock-induced separation of the boundary layer. However, it seems also plausible that the same shock-dominated mechanism, albeit inviscid, that here is observed to cause trailing-edge buzz, could also produce an aileron buzz phenomenon. This question was addressed in Ref. 11, where it was found that such nonclassical (inviscid) buzz phenomena are indeed predicted by the present Euler-based calculations, at Mach numbers very close to those where buzz has been observed in wind tunnel and flight tests. Figure 8 illustrates such a nonclassical aileron buzz instability, as simulated by the present code.

Figure 9 shows the results of flutter simulations for an NACA 0012 model, with typical section parameters similar to those of the NACA 0012 Benchmark Model tested at NASA Langley [25]:

$$a = 0.0$$

$$x_\alpha = 0.0$$

$$r_\alpha^2 = 0.25$$

$$\omega_h/\omega_\alpha = 0.6564$$

Limit cycle flutter is predicted, in a predominantly bending mode, which is in good agreement with the observed flutter at this flutter point. Note the very high mass ratio (4284).

At more realistic mass ratios, our simulations predict a nonlinear interaction between flutter and a weak divergence instability at this same Mach number (0.80), as discussed in Ref. 26. The basic mechanism behind the emergence of this weak divergence, which is quenched by the flutter instability (see Fig. 4 of Ref. 26), is the strong sensitivity of the shocks and the supersonic pockets to relatively small airfoil displacements, as illustrated in Fig. 10. This leads to a symmetry-breaking bifurcation, where the α=0 equilibrium position becomes unstable and bifurcates into two stable nonzero (but small α) equilibrium points.

An example of the Type 2 error discussed in the Introduction is presented in Figs. 11 and 12. At lower transonic Mach numbers, reasonable agreement is observed between the calculated flutter behavior of the NACA 0012 model, using the classical vs. the present calculation approach. In the upper transonic range ($M > 0.9$), however, significant discrepancies were observed. At Mach 0.94, for example, the present simulations indicate that the linear flutter boundary is at around $\bar{U} = 6.1$, with strong flutter already evident at $\bar{U} = 6.5$, as shown in Fig. 11. The classical calculation method predicts *no flutter whatsoever*, for all reduced velocities up through 8.0 (see Fig. 12), and predicts divergence around $\bar{U} = 8.2$–8.5. A doubling of the mesh density and a reduction in the time step used had essentially no effect on the predicted behaviors. The precise reason for this significant difference in predicted aeroelastic behaviors is presently unknown

Transonic Flutter in Cascades and Rotors

Fan and compressor blades are thin, flexible structures, usually of solid titanium or steel, where camber bending is of considerable importance because of the presence of plate-type modes. In addition to being susceptible to a number of different flutter instabilities, all turbomachinery blades are subject to fatigue. It is therefore highly desirable to have flutter and aeroelastic response computational methods based on realistic finite element models for the blades, so that dynamic stresses can be calculated.

In the present flutter simulations, two different structural models are used. In the 2D cascade calculations, we make use of the modified typical section model discussed previously. In this model, the blades are treated as thin isotropic plates of unit width in the spanwise direction, with the typical section stiffness represented by attaching blade bending and torsion springs K_h and K_α at the elastic axis of the blade. The chordwise flexibility (camber bending) of the blade is modeled using several plate elements in the chordwise direction, and the fluid domain is discretized using the finite volume procedure. In the quasi-3D calculations, we make use of the rotating blade model discussed above, and the fluid domain is also solved using finite element discretizations.

Because the blade sections are flexible, the typical section stiffness parameters have been nondimensionalized as follows:

$$\kappa_h = \frac{12c^3 K_h}{Et^3} \quad ; \quad \kappa_\alpha = \frac{12cK_\alpha}{Et^3} \tag{62}$$

where t is the maximum thickness of the blade section. Standard sea level values for the inlet static pressure and density are used, and the blade material is titanium. Using Eq. (62), the bending-torsion frequency ratio can be expressed as

$$\frac{\omega_h}{\omega_\alpha} = \frac{r_\alpha}{2}\sqrt{\frac{\kappa_h}{\kappa_\alpha}} \tag{63}$$

where r_α is the radius of gyration of the blade section about the elastic axis, nondimensionalized by the semichord b. Furthermore,

$$\omega_h = \frac{a_\infty}{c}\sqrt{\frac{E\kappa_h}{3\pi\mu\gamma}\left(\frac{t}{c}\right)^3} \tag{64}$$

where a_∞ is the free-stream speed of sound, γ is the ratio of specific heats, E is Young's modulus, and $\mu = m/(\pi\rho b^2)$ is the mass ratio of the blade.

Unstaggered cascades represent perhaps the best test cases for code checkout and validation purposes, because of their simple geometry and boundary conditions. Linear theory predicts that the critical interphase angle for flutter of an unstaggered cascade is $\sigma = 180$ deg; that is, adjacent blades are in anti-phase motion with respect to each other. The boundary conditions at the channel side boundaries thus become simply the condition for tangent flow, i.e., $v = 0$. This boundary condition remains exact in the nonlinear case, under the assumption that the 180-deg mode is realizable and corresponds to the least stable interblade phase angle.

An illustration of limit cycle flutter in cascades is presented in Fig. 13. After a slight overshoot, the blade settles into a stable limit cycle. Part a) of this figure shows the transverse bending displacement $w = -h/c$ (nondimensionalized by the chord $c = 2b$) at the elastic axis, and the local rotational displacement θ about this axis. Note that $\theta = -\alpha$ if camber bending is neglected. Part b) shows the corresponding nondimensional total energy, $E_{tot} = U + T$, of the blade section vs. time, and the work W_A done by the fluid pressure on all the finite elements making up the blade section. Also plotted is the difference $E_{tot} - W_A$, which in the present undamped model should equal to a constant, i.e., the initial energy of the blade. By integrating the energy equation, we obtain an independent check on the accuracy of our method and the

Runge-Kutta integration scheme. Note the excellent agreement between the initial energy and the difference $E_{tot} - W_A$, over more than 20 flutter cycles of oscillation, representing roughly 50,000 time steps. This attests to one of the important advantages of the present method in aeroelastic calculations; namely, the fidelity by which the transfer of energy (and therefore also momentum) between the fluid and the structure is reproduced. The C_p behavior during flutter is shown in Fig. 14, which reveals a significant shock motion, of the order of the blade chord.

Figure 15 illustrates the emergence of a "nonclassical" flutter mode in a staggered cascade of NACA 0006 blades, operating at an angle of attack of 3 degrees and at a Mach number of 0.85. The interblade phase angle is zero. In this example, the bending and torsion modes interact nonlinearly to yield a flutter mode that is not a simple, exponentially growing sinusoid. Instead, the flutter time history reveals a regular pattern that repeats (with increasing amplitudes) every 3 cycles. Within the 3-cycle pattern, the bending-torsion amplitude ratio changes over a significant range, $h/b\alpha \approx 0.2$–0.7. This suggests a nonlinear interaction between the bending and torsion modes, wherein energy is continually exchanged between the two modes. Although the flutter mode is not a "classical" flutter mode, it is nevertheless a clearly defined coherent aeroelastic mode. The blades undergo significant camber bending during flutter.

For the staggered NACA 0006 cascade considered in Fig. 15, an increase in the Mach number from 0.85 to 0.90 turned out to be stabilizing, leaving the blade essentially on the flutter boundary, as illustrated in Fig. 16. Again, a highly nonlinear flutter mode emerges.

Finally, an unstaggered cascade of rotating low-aspect-ratio NACA 0003 blades is shown in Fig. 17. Such blade sections may be considered representative of the aft stages of compressor rotors, or of the thin tip region of advanced fan blades, outboard of the shrouds. Figures 17a) and 17b) show the aeroelastic response in bending and torsion, respectively. Here, the angle of twist of the blade is defined as

$$\theta_x = (w_{TE} - w_{LE})/c \tag{65}$$

and is equivalent to the conventional torsion theory definition when the blade is chordwise rigid. Both figures reveal an increase of the amplitude of motion vs. time, *i.e.*, flutter, and a coherent aeroelastic mode emerges as the blade becomes unstable. The energy plot is illustrated in Fig 17c) and shows that a large amount of energy is extracted by the blade from the fluid, indicating explosive flutter.

Transonic Panel Flutter

Nonlinear panel flutter in the supersonic range has been studied by a number of researchers, using a variety of unsteady aerodynamic theories (for an excellent review of the subject, see Dowell [27]). It is well-known that linear aerodynamic theories give reasonable agreement with experiments for Mach numbers above about 1.3-1.4, but give poor agreement in the transonic range, $1 \le M < 1.3$.

One obvious reason for this discrepancy could be that nonlinear aerodynamic effects *are* important and need be included. Recent simulations using the present computational model [10] suggest that the nonlinear aerodynamic characteristics of transonic flows, including moving shocks and embedded subsonic regions, may also give rise to a change in the flutter mode from a standing to a traveling wave. It was noted by Dowell [27] that in the low supersonic (transonic) region, the flutter mode predicted by linearized aerodynamic theories is essentially a single-degree-of-freedom mode. However, the present nonlinear calculations using Euler-based aerodynamics predict traveling wave flutter modes in the transonic Mach number range.

Figures 18 and 19 show the panel deflections at 1/4-chord, midchord, and 3/4-chord during limit cycle flutter of a typical panel at Mach numbers of 1.0 and 1.2, respectively. The motion of the panel at Mach 1 is especially irregular (but periodic) and shows significant phase differences between the deflections of the panel at different chord locations, indicating the presence of a traveling wave (in the generalized sense used by Dowell). The direction of propagation of

the wave is in the direction of flow, in agreement with experimental observations. A snapshot of the panel deflection and the associated Mach number distribution, Fig. 20, clearly shows the presence of a strong shock on the panel.

When the Mach number was increased to 1.2, the strong shocks disappeared and the limit cycle flutter became more "regular", Fig. 19. However, the presence of higher harmonics in the flutter response is still evident, as is the temporal phase shifts between the various points along the plate chord. Figure 21 presents a series of snapshot plots of the panel deflection during one period of limit cycle oscillation. It is interesting to note that the "instantaneous mode shape" continuously evolves during each cycle of oscillation, in a nonharmonic manner. Again, the flutter mode must be classified as a traveling wave, in the generalized sense.

SUMMARY AND CONCLUSIONS

An overview of a new method for simulating the aeroelastic response of a diverse class of systems has been presented, and the advantages of the new scheme in actual flutter calculations have been explored. The method has number of important advantages over existing methods. Realistic finite element models can be introduced, without first solving large eigenvalue problems to obtain the normal modes. This modeling can be done at the *element* level, using existing finite element libraries. No assembly of mass and stiffness matrices into global (system) matrices is required, hence there is no need to introduce special procedures for dealing with sparse matrices. Results indicate that the new computational scheme is capable of reproducing the energy exchange between the fluid and the structure with significantly less error than existing methods.

Because no global mass and stiffness matrices are assembled for the structure, the actual dynamics simulated by the present method differs from what would be calculated by classical modal methods. The present method simulates the local force and momentum transfer between individual elements, in the time domain, and is therefore able to model wave propagation phenomena that most modal methods are ill-equipped to do. Because the flutter mode emerges as part of the solution, as it would in a flutter test, there is no need to worry about "how many" and "which" modes should be kept in the flutter analysis.

The importance of camber bending in certain transonic flutter problems has been illustrated, including a new trailing-edge "buzz" phenomenon that is predicted to occur if the chordwise stiffness is sufficiently low, and a nonclassical (inviscid) form of aileron buzz. Nonlinear aeroelastic modes, where two or more degrees-of-freedom exchange energy in a nonstationary manner during flutter, have been observed in numerical simulations of transonic flutter in cascades. No linear theory can be expected to provide an adequate theoretical basis for analyzing such phenomena. In some of these problems, many degrees of freedom participate, making classical modal method less efficient. It is precisely in such problems that the advantages of the present method are brought out. For example, the possibility of considering *traveling wave* flutter modes without special advance set-up is an obvious advantage, as demonstrated in the transonic panel flutter solutions.

ACKNOWLEDGEMENTS

This research was supported by NASA Dryden Grant NCC 2-374, and by NASA Lewis Research Center Contracts NAS3-25574 and NAS3-26064. The author wishes to acknowledge the help of two of his Ph.D. students, Dr. C. Hsiao and Mr. G. Davis, in carrying out some of the computational simulations presented in this paper.

REFERENCES

1. Theodorsen, T., "General Theory of Aerodynamic Instability and the Mechanism of Flutter," *NACA Rept. 496*, 1935.
2. Scanland, R.H. and Rosenbaum, R., *Introduction to the Study of Aircraft Vibration and Flutter*, The Macmillan Co., New York, NY, 1951.
3. Bisplinghoff, R.L., Ashley, H. and Halfman, R., *Aeroelasticity*, Addison-Wesley Publishing Co., Cambridge, MA, 1955.
4. Fung, Y.C., *An Introduction to the Theory of Aeroelasticity*, John Wiley and Sons, Inc., New York, NY, 1955.
5. Dowell, E.H., et al., *A Modern Course in Aeroelasticity*, Sijthoff & Noordhoff, Alphen aan den Rijn, The Netherlands, 1978.
6. Bendiksen, O. O., "A New Approach to Computational Aeroelasticity," AIAA Paper 91-0939, *Proc. AIAA/ASME/ASCE/AHS/ASC 32nd Structure, Structural Dynamics and Materials Conf.*, Baltimore, MD, April 8-9, 1991, pp. 1712-1727.
7. Bendiksen, O.O., "A Mixed Eulerian-Lagrangian Computational Method for Flutter Calculations" Paper 91-091, presented at the *International Forum on Aeroelasticity and Structural Dynamics 1991*, Aachen, Germany, June 3-6, 1991.
8. Bendiksen, O.O., "Numerical Simulations of Unsteady Flow and Flutter in Transonic Cascades," *Sixth Int. Symposium on Unsteady Aerodynamics, Aeroacoustics and Aeroelasticity of Turbomachines and Propellers*, Univ. of Notre Dame, IN, Sept. 15-19, 1991.
9. Hsiao, C. and Bendiksen, O.O., "Finite Element Euler Calculations of Transonic Flutter in Cascades," AIAA Paper 93-2083, *29th AIAA/ASME/SAE/ASEE Joint Propulsion Conf.*, Monterey, CA, June 28-30, 1993.
10. Davis, G.A. and Bendiksen, O.O., "Transonic Panel Flutter," AIAA Paper 93-1476, *AIAA/ASME/ASCE/AHS/ASCE 34th SDM Conf.*, La Jolla, CA, April 19-22, 1993.
11. Bendiksen, O.O., "Nonclassical Aileron Buzz in Transonic Flow," AIAA Paper 93-1479, *AIAA/ASME/ASCE/AHS/ASCE 34th SDM Conf.*, La Jolla, CA, April 19-22, 1993.
12. Seliger, R.L. and Whitham, G.B, "Variational Principles in Continuum Mechanics," *Proc. Royal Society, Series A*, Vol. 305, 1968, pp. 1-25.
13. Lamb, H., *Hydrodynamics*, 6th ed., Cambridge University Press, 1932.
14. Hedstrom, G. W., "Nonreflecting Boundary Conditions for Nonlinear Hyperbolic Systems," *Journal of Computational Physics*, Vol. 30, 1979, pp. 222-237.
15. Jameson, A. and Venkatakrishnan, V., "Transonic Flows About Oscillating Airfoils Using the Euler Equations," AIAA Paper 85-1514-CP, July 1985.
16. Jameson, A. and Baker, T. J., "Solution of the Euler Equations for Complex Configurations," *Proc. AIAA 6th Computational Fluid Dynamics Conference*, Danvers, MA, 1983, pp. 293-302.
17. Mavriplis, D. "Solution of the Two-Dimensional Euler Equations on Unstructured Triangular Meshes," Ph.D. Dissertation, Department of Mechanical and Aerospace Engineering, Princeton University, Princeton, NJ, 1987.
18. Davis, G.A. and Bendiksen, O.O., "Unsteady Transonic Two-Dimensional Euler Solutions Using Finite Elements," *AIAA Journal*, Vol. 31, June 1993, pp. 1051-1059.
19. Hsiao, C. and Bendiksen, O. O., "Finite Element Euler Calculations of Unsteady Transonic Cascade Flows," AIAA Paper 92-2120, *Proc. AIAA Dynamics Specialists Conf.*, Dallas, TX, April 16-17, 1992, pp. 389-400.
20. Bendiksen, O. O., and Hsiao, C., "New Computational Method for Aeroelastic Problems in Turbomachines," University of California Report UCLA-ENG-93-14, Department of

Mechanical, Aerospace and Nuclear Engineering, April, 1993.
See also Hsiao, C. "Mixed Eulerian-Lagrangian Finite Element Solutions of Unsteady Flow and Flutter in Transonic Cascades," Ph. D. Dissertation, Department of Mechanical, Aerospace, and Nuclear Engineering, University of California, Los Angeles, 1993.

21. Davis, G.A. and Bendiksen, O.O., "Transonic Panel Flutter," revised version of Ref. 10, in preparation.
22. Kousen, K.A. and Bendiksen, O.O., "Nonlinear Aspects of the Transonic Aeroelastic Stability Problem," AIAA Paper 88-2306, *Proc. AIAA/ASME/ASCE/AHS/ASCE 29th SDM Conf.*, Williamsburg, VA, April 18-20, 1988, pp. 760-769.
23. Kousen, K.A. and Bendiksen, O.O., "Limit Cycle Phenomena in Computational Transonic Aeroelasticity," AIAA Paper 89-1185, *Proc. AIAA/ASME/ASCE/AHS/ASCE 30th SDM Conf.*, Mobile, AL, April 3-5, 1989, pp. 230-240.
24. Ashley, H., "Role of Shocks in the 'Sub-Transonic' Flutter Phenomenon," *Journal of Aircraft*, Vol. 17, March 1980, pp. 187-197.
25. Rivera, J.A., et al., "NACA 0012 Benchmark Model Experimental Flutter Results with Unsteady Pressure Distributions," *NASA TM 107581*, March 1992.
26. Bendiksen, O.O., "Role of Shock Dynamics in Transonic Flutter," AIAA Paper 92-2121, *Proc. AIAA Dynamics Specialist Conf.*, Dallas, TX, April 16-17, 1992, pp. 401-414.
27. Dowell, E.H., "Panel Flutter: A Review of the Aeroelastic Stability of Plates and Shells," *AIAA Journal*, Vol. 8, March 1970, pp. 385-399.

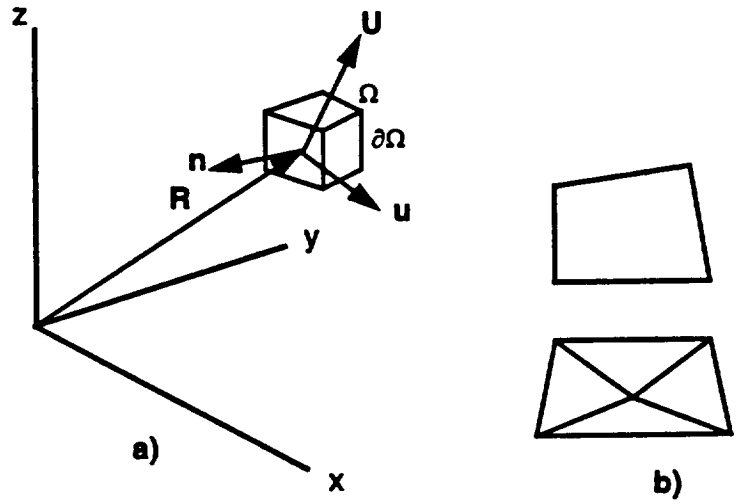

Fig. 1 Coordinate system and typical 2D and 3D elements

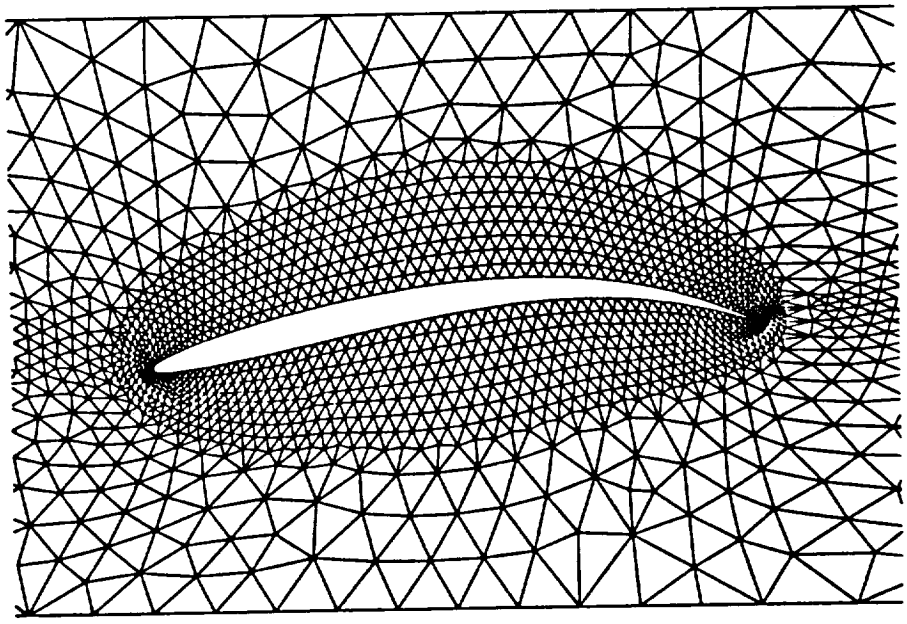

Fig. 2a Hybrid cascade mesh (reference channel, near field)

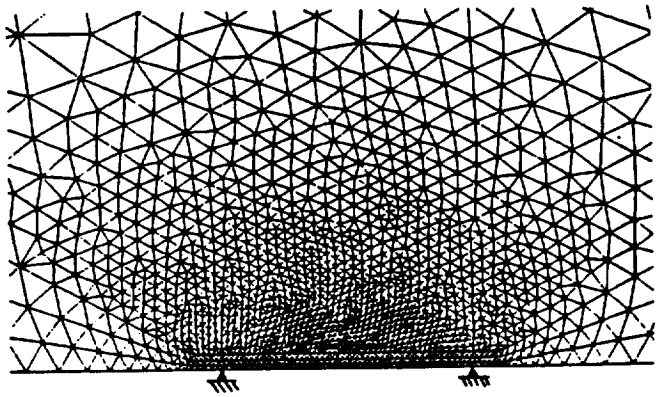

Fig. 2b Unstructured mesh used in panel flutter calculations (near field)

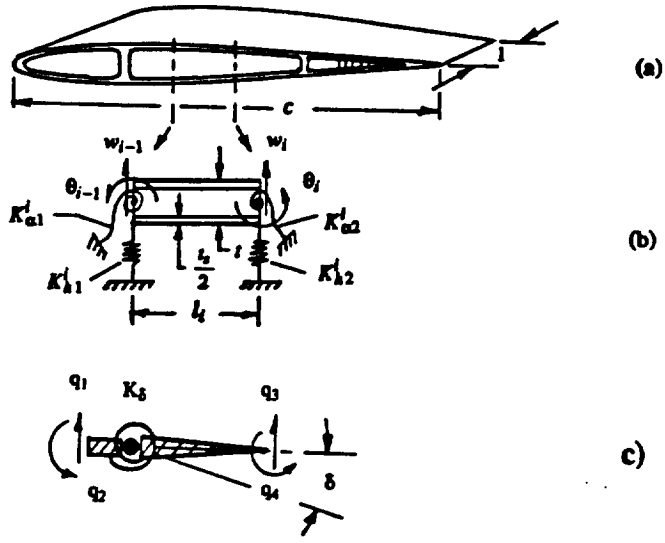

Fig. 3 a) Modified typical section wing model with camber bending
b) Basic finite element
c) Aileron hinge element

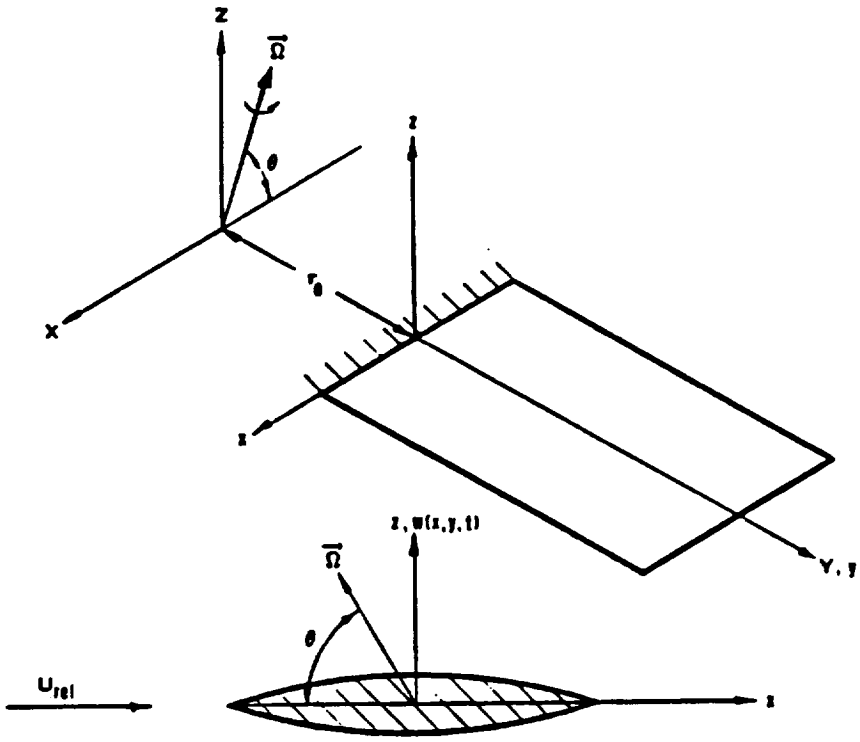

Fig. 4a Rotating turbomacinery blade

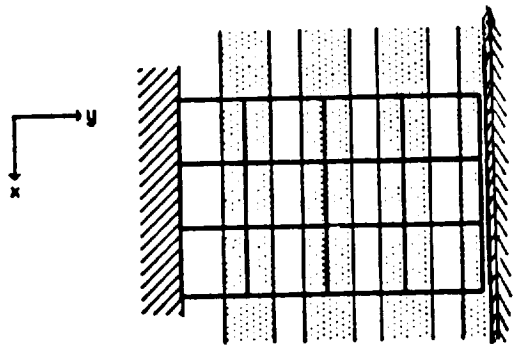

Fig. 4b Quasi-3D aeroelastic model, with aerodynamic channels shaded

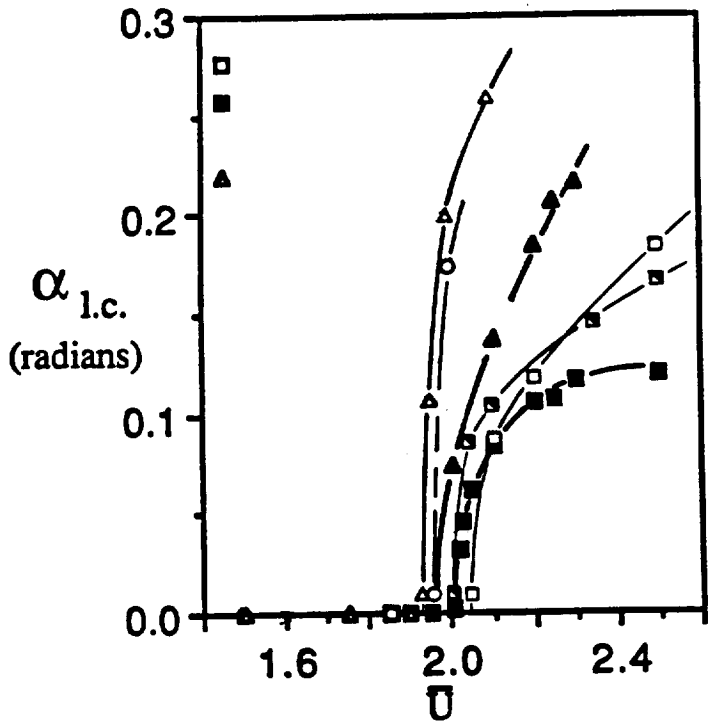

Fig. 5 Bifurcation diagram for the NACA 64A006 wing model, as calculated by present method and compared with Ref. 22:
M = 0.87: ▲ --- Ref. 22; Present method: △ --- $t_s/t = 0.05$; ○ --- $t_s/t = 0.25$
M = 0.92: ■ --- Ref. 22; Present method: □ --- $t_s/t = 0.05$; ◪ --- $t_s/t = 0.10$

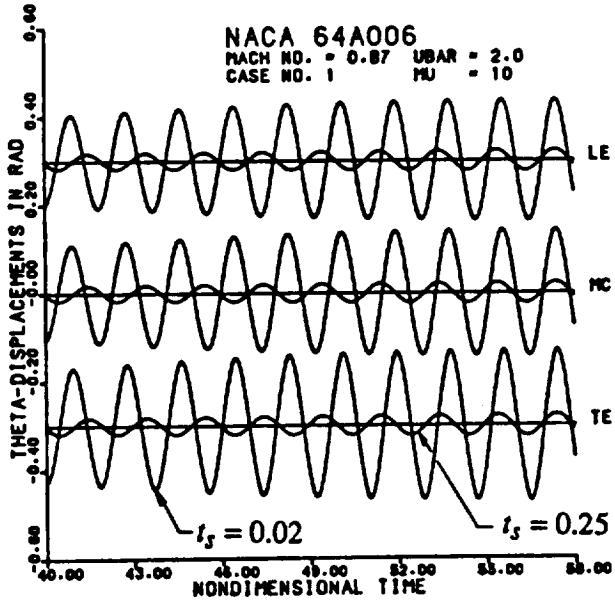

Fig. 6 Effect of chordwise flexibility on transonic limit cycle flutter at Mach 0.87

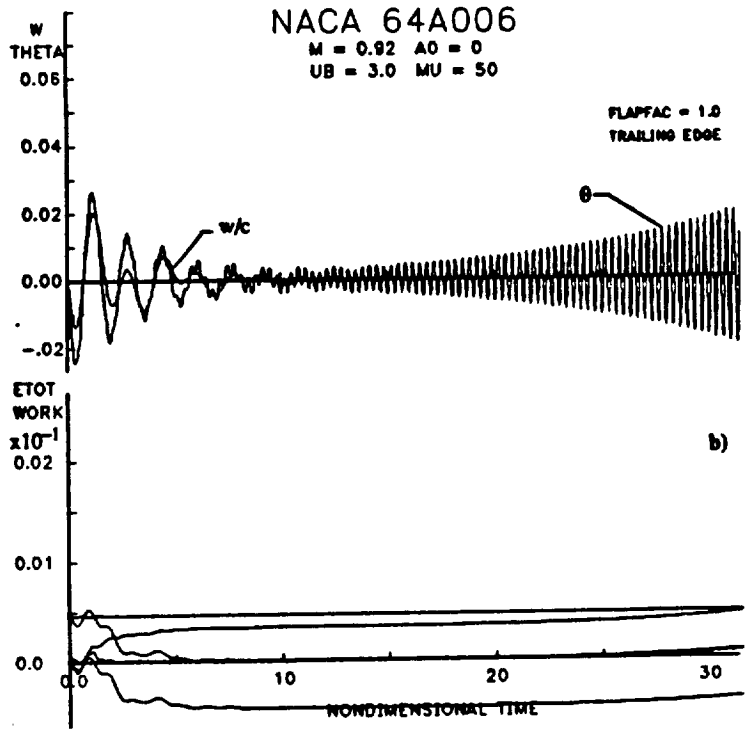

Fig. 7 Transition to localized trailing edge buzz mode
($t_s/l = 0.10$; $\bar{U} = 3.0$; $M = 0.92$)

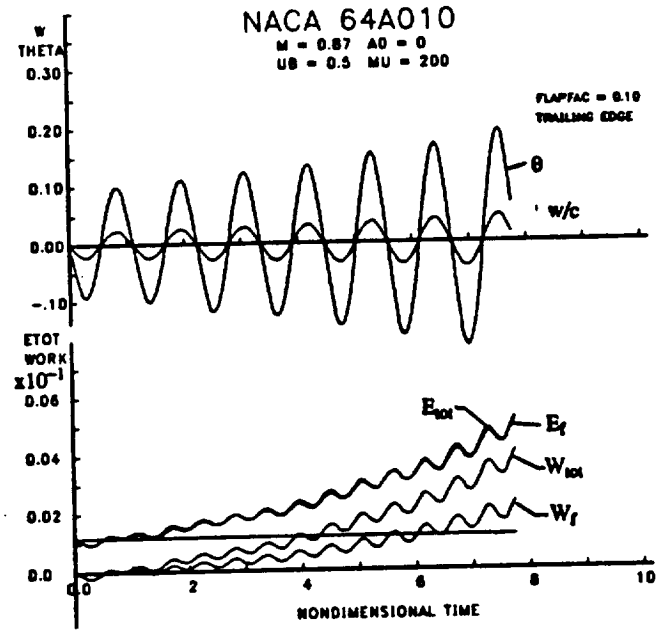

Fig. 8 Nonclassical Type B buzz (nonzero hinge stiffness)

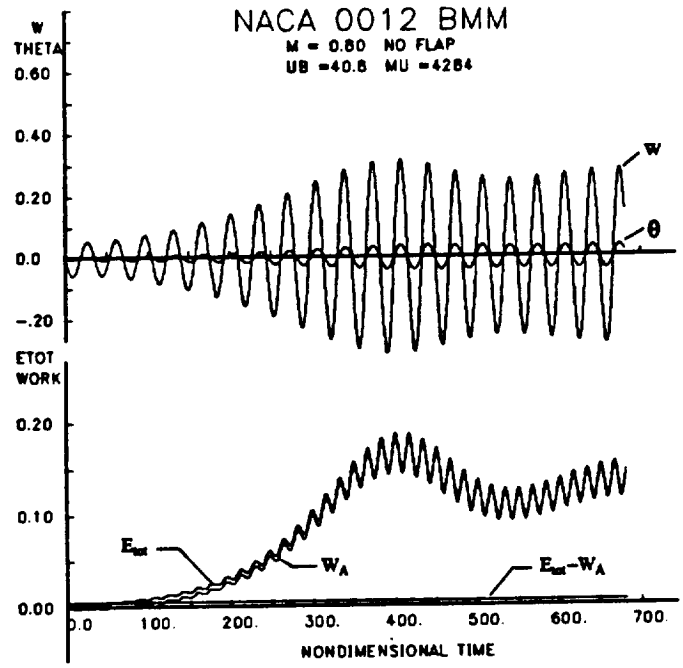

Fig. 9 Hopf bifurcation to transonic limit cycle flutter of NACA 0012 model at Mach 0.80 and high mass ratio ($\mu = 4284$)

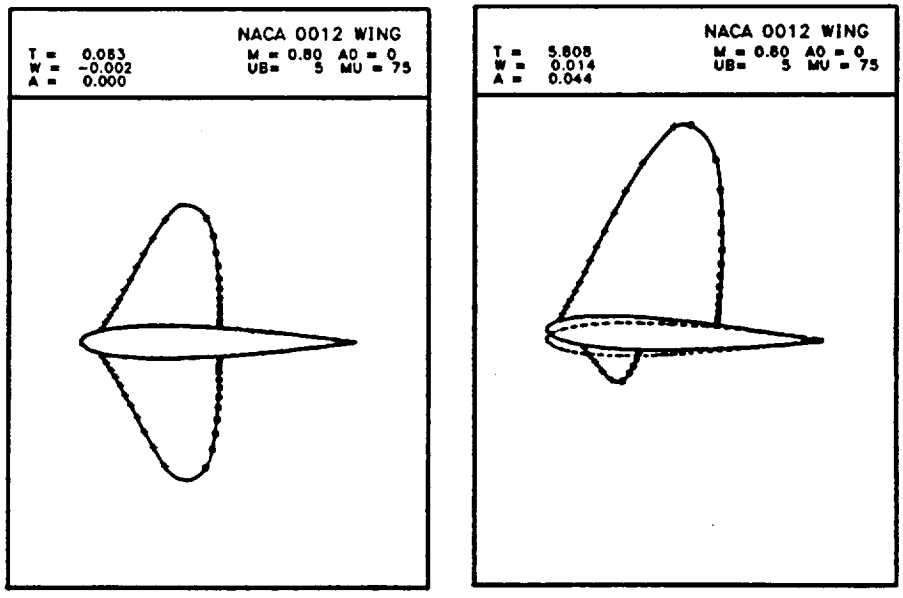

Fig. 10 Motion of supersonic pockets and shocks during symmetry-breaking bifurcation that gives rise to weak divergence and flutter-divergence interactions at Mach 0.80 and μ=75

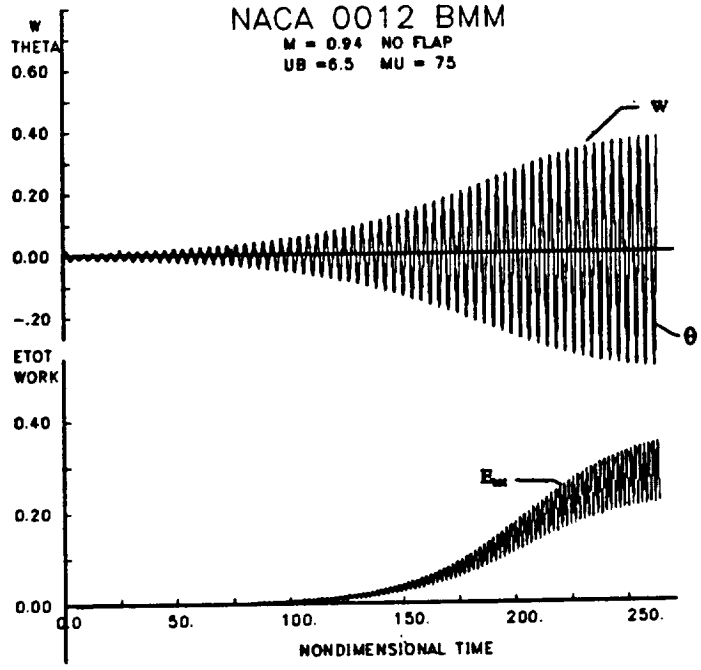

Fig. 11 Strong flutter of NACA 0012 model at Mach 0.94 and $\bar{U} = 6.5$, as calculated by present scheme. Classical scheme fails to predict flutter for this Mach number (see Fig. 12) and predicts divergence for $\bar{U} \geq 8.3$. Present scheme predicts no divergence-flutter interactions until $\bar{U} \geq 11$

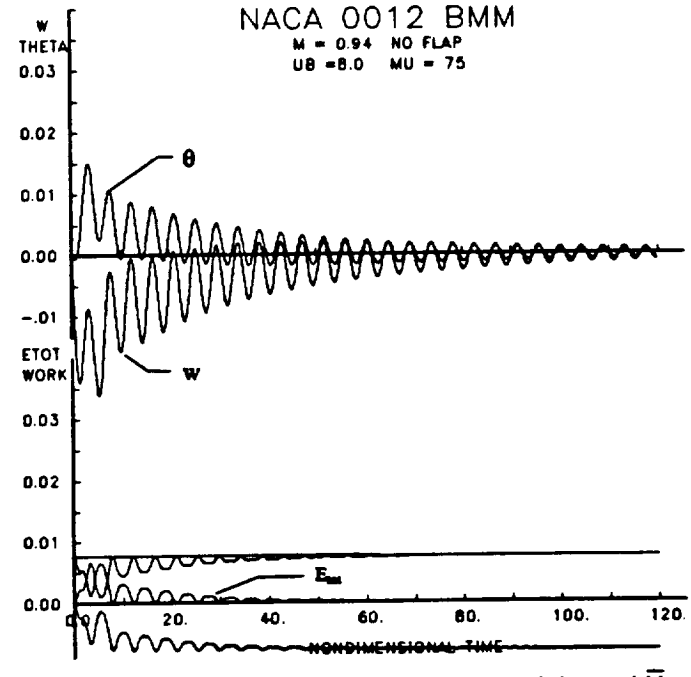

Fig. 12 Stable response of NACA 0012 model at Mach 0.94 and $\bar{U} = 8.0$, as calculated by classical scheme. Classical scheme fails to predict flutter for this Mach number, up to the divergence boundary, in sharp contrast to the predictions of the new scheme

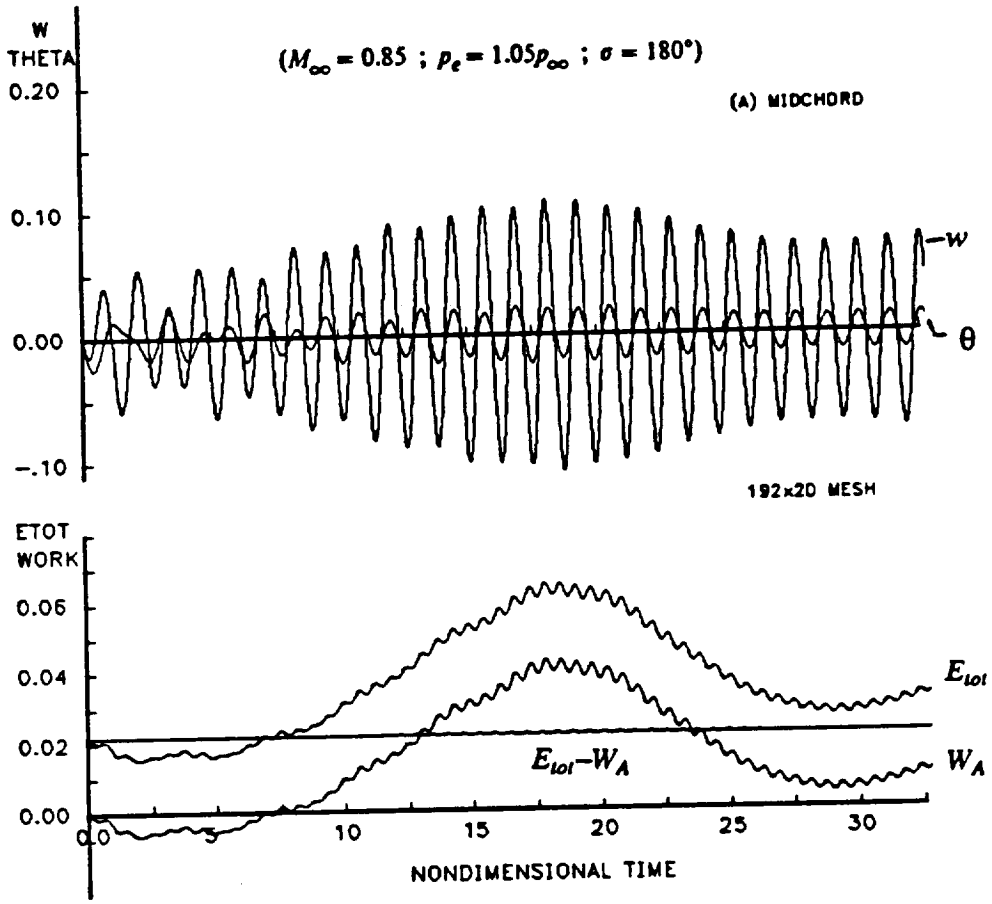

Fig. 13 Limit cycle flutter of unstaggered NACA 0006 cascade at Mach 0.85
($s/c = 1$; $\kappa_h = 3.0$; $\kappa_\alpha = 0.4$; EA at 0.512c)

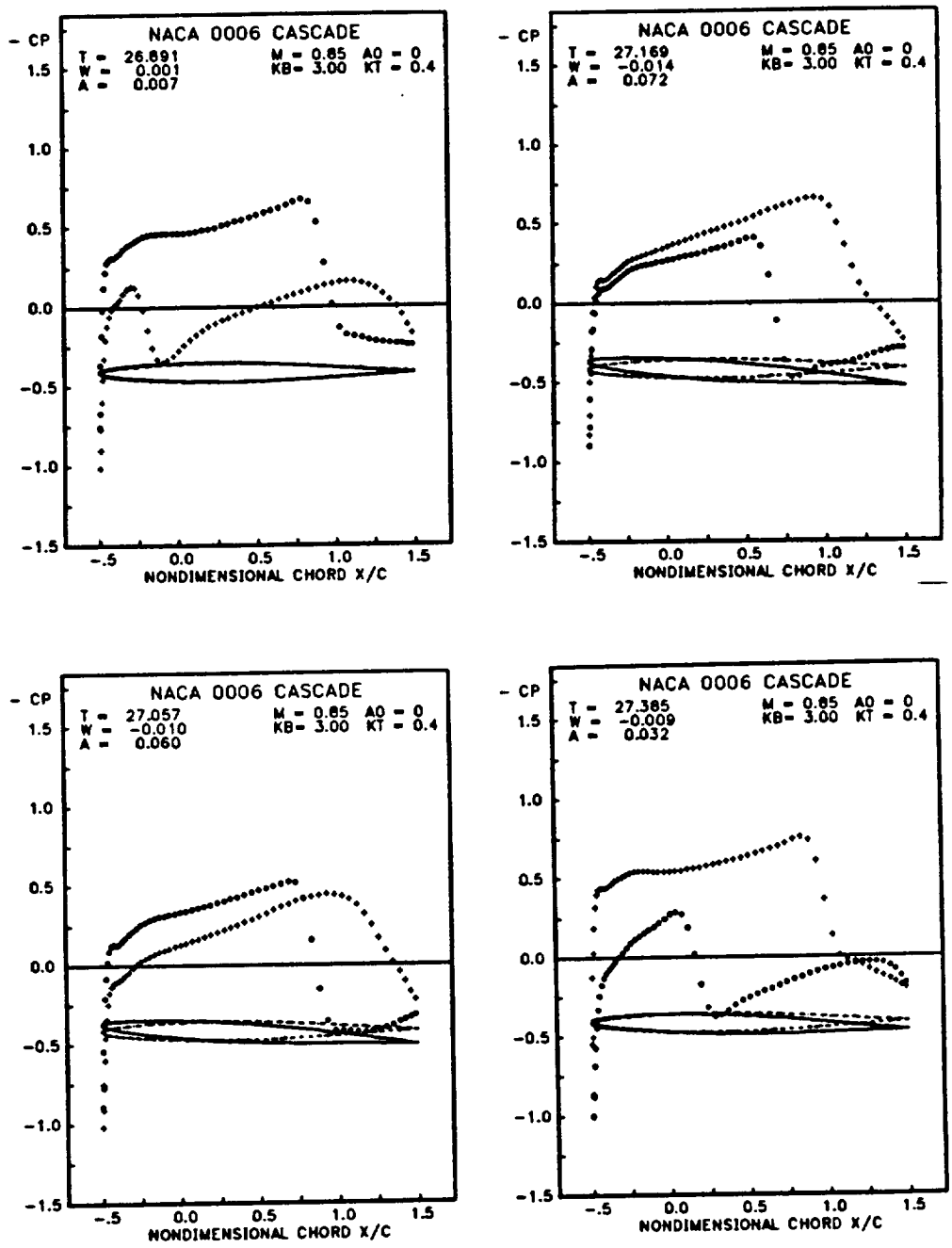

Fig. 14 Blade pressure coefficient C_p during limit cycle flutter shown in Fig. 13

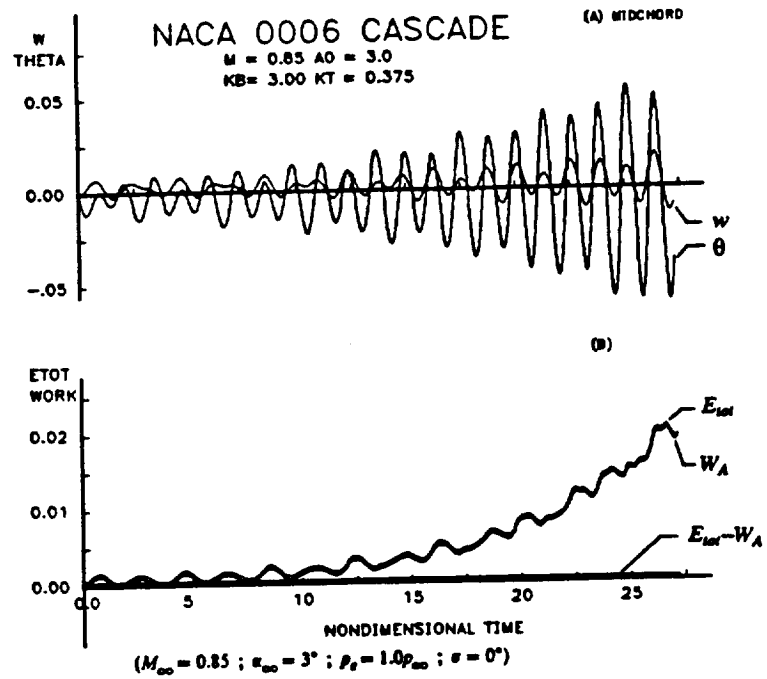

Fig. 15 Nonlinear (nonclassical) bending-torsion flutter of NACA 0006 cascade with $\theta = 45$ deg; $s_2/c = 1$; $\kappa_h = 3.0$; $\kappa_\alpha = 0.375$; EA at 0.512c

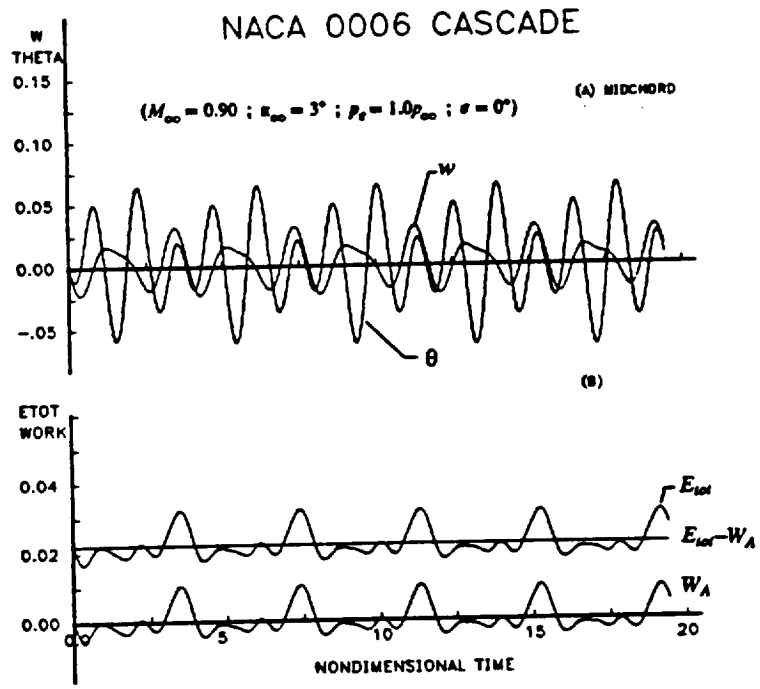

Fig. 16 Highly nonlinear flutter at Mach 0.90 of cascade in Fig. 15. Note stabilizing effect of increasing Mach number from 0.85 to 0.90

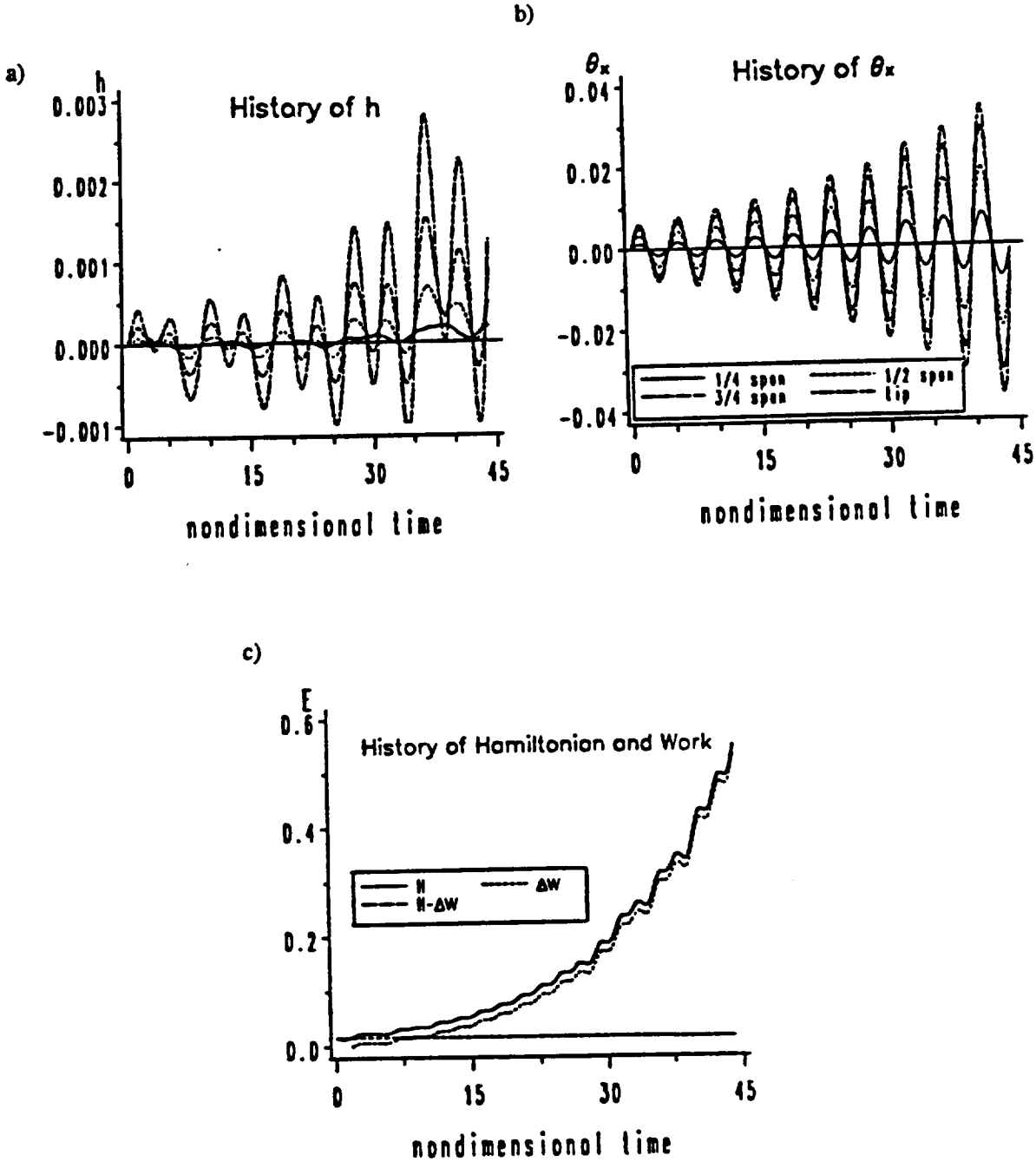

Fig. 17 Explosive flutter of a rotating NACA 0003 blade in an unstaggered cascade: a) plunging motion (at EA); b) angle of twist; c) Hamiltonian and work done by aerodynamic forces ($s/c = 1$, $M_\infty = 0.85$, $\sigma = 180$ deg, $L/c = 1$)

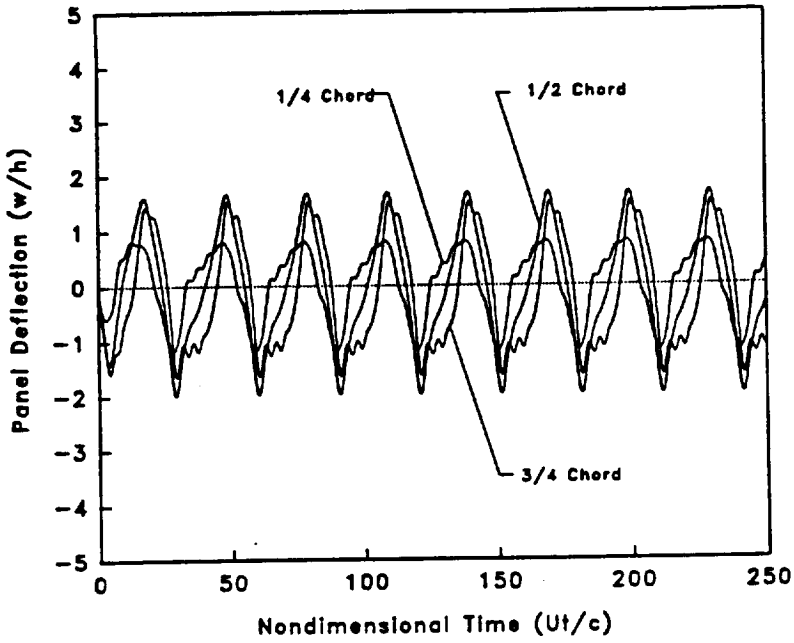

Fig. 18 Transonic limit cycle panel flutter at Mach 1.0, illustrating highly irregular (but periodic) aeroelastic response and evidence of a traveling wave. Simply supported aluminum panel at 20,000 ft altitude; h/c = 0.004

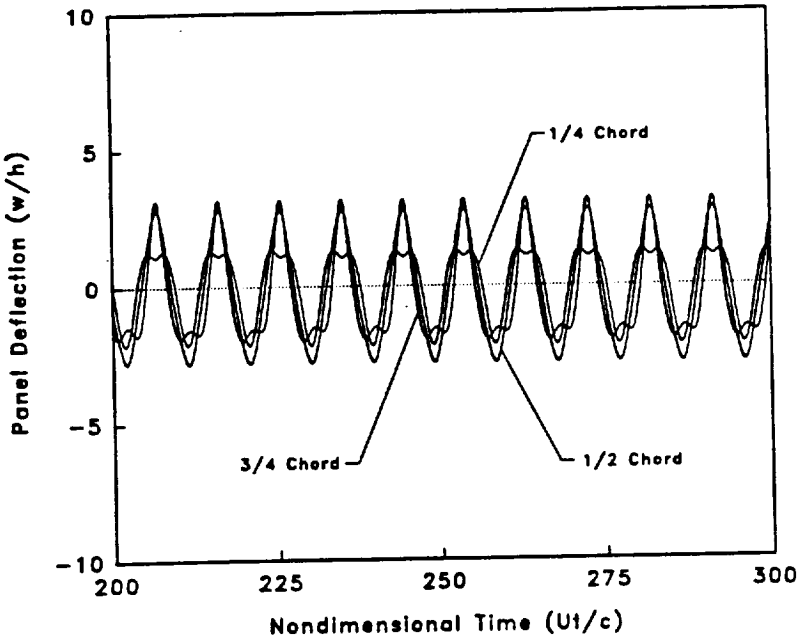

Fig. 19 Transonic panel flutter at Mach 1.2 of same panel as in Fig. 18. Initial transient response is not shown

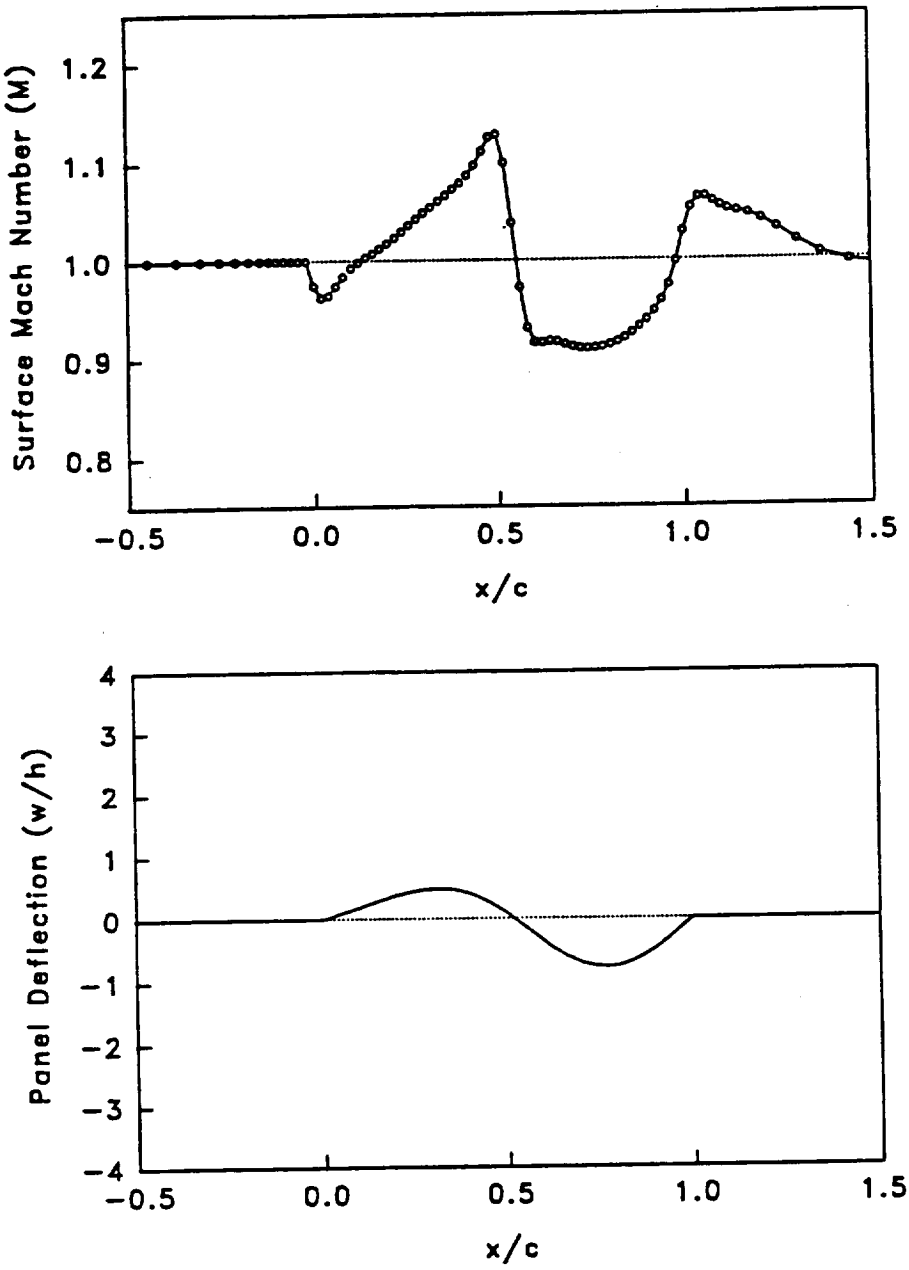

Fig. 20 Snapshot of panel deflection and corresponding Mach number distribution during limit cycle flutter at Mach 1 (Fig. 18). Flutter mode is a traveling wave and a strong shock is present on the panel surface

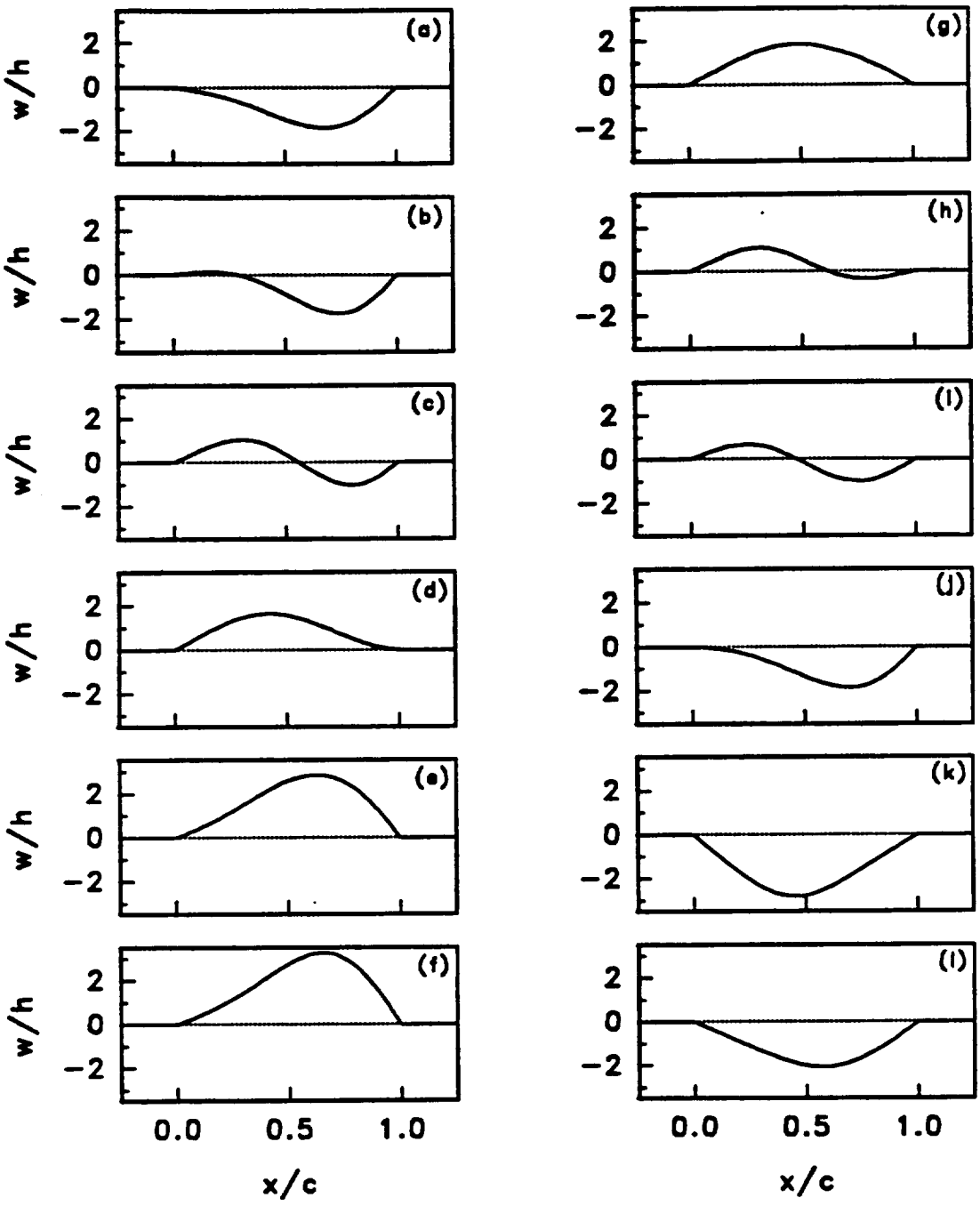

Fig. 21 Snapshots of panel flutter mode shape at different times during one cycle of flutter of panel at Mach 1.2, corresponding to Fig. 19